

SN 2022joj

CHANG LIU ^{1,2} ADAM A. MILLER ^{1,2} AND FANTASTIC ASTRONOMERS

¹*Department of Physics and Astronomy, Northwestern University, 2145 Sheridan Rd, Evanston, IL 60208, USA*

²*Center for Interdisciplinary Exploration and Research in Astrophysics (CIERA), Northwestern University, 1800 Sherman Ave, Evanston, IL 60201, USA*

ABSTRACT

Keywords: Supernovae (1668), Type Ia supernovae (1728), White dwarf stars (1799), Observational astronomy (1145), Surveys (1671)

1. INTRODUCTION

Type Ia supernovae (SNe Ia) are known to result from thermonuclear explosions of C/O white dwarfs (WDs) in binary systems, yet it remains highly uncertainty how the WDs get ignited or what the roles their companions are playing in the ignition (see Maoz et al. 2014; Liu et al. 2023b, for a review). Multiple explosion channels have been proposed, none of which is able to fully explain the diversity in the SN Ia population.

The helium-shell double detonation (DDet) scenario is one of the most intriguing explosion mechanisms. In a DDet, the detonation of a helium shell (from a helium-rich companion) atop the primary WD sends a shock wave inward, which eventually converges near the center of the C/O core, triggers a secondary detonation, and inevitably destroys the entire WD (Nomoto 1982a,b; Woosley et al. 1986; Livne 1990; Woosley & Weaver 1994; Livne & Arnett 1995). This mechanism can dynamically ignite WDs well below the M_{Ch} . It has been proposed in a couple of independent studies that a substantial fraction of SNe Ia could result from DDets, including the studies on the intrinsic event rates and delay-time distributions (DTDs) of the SN Ia population () and the nucleosynthesis yields of SNe Ia measured in their late-time spectra (Maguire et al. 2018; Flörs et al. 2020) or from the chemical enrichment history of various galaxies (de los Reyes et al. 2020; Sanders et al. 2021; Eitner et al. 2022).

The remarkable observational properties for SNe Ia from DDet are mostly associated with the helium shell. Shortly after the shell detonation, the decay of the radioactive species synthesized during the helium burning may power a flux excess in the early light curves (Woosley & Weaver 1994; Fink et al. 2010; Kromer et al. 2010). Afterwards, the iron-group elements (IGEs) in the helium ashes may blanket photons with wave-

lengths bluewards of $\sim 5000 \text{ \AA}$ (Kromer et al. 2010), efficiently suppressing the flux in blue. In general, progenitors with a thin helium shell would show minimal detectable effects from the shell detonation, and reproduce “normal” luminosity and spectroscopic properties around maximum luminosity (e.g., Townsley et al. 2019; Magee et al. 2021; Shen et al. 2021b). Normal SNe Ia with a red flux excess shortly after the explosion may be associated with this scenario (e.g., SN 2018aoz; Ni et al. 2022). Meanwhile, objects involving a more massive helium shell would exhibit peculiarities, such as a strong flash at early times and an extremely red color around maximum luminosity (Polin et al. 2019). A few of the weirdo SNe Ia are interpreted as peculiar DDet SNe, including OGLE-2013-SN-079 (Inserra et al. 2015), SN 2016dsg (Dong et al. 2022), SN 2016hmk (Jacobson-Galán et al. 2020; but see Galbany et al. 2019 for an alternative interpretation), SN 2016jhr (Jiang et al. 2017), SN 2018byg (De et al. 2019), SN 2019eix (Padilla Gonzalez et al. 2023), SN 2019ofm (De et al. 2020), and SN 2020jgb (Liu et al. 2023a).

More complexities arise due to the fact that DDets are intrinsically multidimensional and the ejecta are highly asymmetric. As a result, all the observables (e.g., luminosities, colors, and absorption line features) are subject to the viewing angles of observers (Fink et al. 2010; Shen et al. 2021b). The asymmetries of the element distribution in the SN Ia ejecta have been indicated in SN spectropolarimetric measurements () and in systematic studies on the kinematics of Si and Fe (Maeda et al. 2010; Maguire et al. 2018; Li et al. 2021). To accurately estimate the progenitor properties for a DDet SN, one needs to compare the observations to a series of multi-dimensional models viewed from a range of orientations and find a reasonable match.

In this paper, we present observations of a peculiar SN Ia, SN 2022joj. SN 2022joj shows a remarkable color evolution, starting with a red color which quickly turns into blue as it rises to its maximum luminosity. Its photometric and spectroscopic features are qualitatively consistent with that of a peculiar DDet SNe. In Section 2, we report the observations of SN 2022joj, which are analyzed in Section 3, where we show its peculiarities in various aspects. In Section 4.1, we discuss existing scenarios that can lead to a red color in the early light curves of a SN Ia, in which the helium-shell DDet scenario is the most reasonable explanation. We also show that multidimensional effects have to be accounted for to explain the spectroscopic peculiarities. The indication of a sub- M_{Ch} progenitor and an asymmetric explosion is supported by the late-time spectra of SN 2022joj, which is discussed in Section 4.2. We draw our conclusions in Section 5.

2. OBSERVATIONS

2.1. Discovery & Classification

SN 2022joj was discovered by the Zwicky Transient Facility (ZTF; Bellm et al. 2019a; Graham et al. 2019; Dekany et al. 2020) on 2022 May 08.298 (UT dates are used throughout the paper; MJD 59707.298) with the 48 inch Samuel Oschin Telescope (P48) at Palomar Observatory. It was detected with $r_{\text{ZTF}} = 19.13 \pm 0.06$ mag at $\alpha_{\text{J2000}} = 14^{\text{h}}41^{\text{m}}40^{\text{s}}.08$, $\delta_{\text{J2000}} = +03^{\circ}00'24''.14$ and announced to the public by Fremling (2022). SN 2022joj was detected via the ZOGY image differencing algorithm (Zackay et al. 2016), which is utilized by the automated ZTF discovery pipeline (Masci et al. 2019). A real-time alert (Patterson et al. 2019) was generated as the candidate passed internal machine-learning thresholds (e.g., Duev et al. 2019; Mahabal et al. 2019), and the internal designation ZTF22aaajijf was assigned. The last $3\text{-}\sigma$ nondetection limits the brightness to $r_{\text{ZTF}} > 21.48$ mag on 2022 May 03.27 (MJD 59702.27; 5.03 days before the first detection) using the ZTF forced photometry from the ZTF Forced Photometry Service (ZFPS; Masci et al. 2023). SN 2022joj was also independently monitored by Asteroid Terrestrial-impact Last Alert System (ATLAS; Tonry et al. 2018). The last $3\text{-}\sigma$ nondetection with ATLAS was on 2022 May 04.26, 0.99 days after the last nondetection in r_{ZTF} , and with the forced photometry we put a limit of brightness in the orange filter of $o > 19.84$ mag.

The first spectrum was obtained on 2022 May 11.288 by Newsome et al. (2022), who found a best fit to a young Type I SN at $z = 0.03$ using the Supernova Identification (SNID) algorithm (Blondin & Tonry 2007). In this early spectrum, prominent Si II $\lambda 6355$ and

Ca II infrared triplet (IRT) absorption suggest a SN Ia classification, but the overall spectral shape, featuring a relatively red continuum (see Figure 2), is atypical for a normal SN Ia at this phase. Chu et al. (2022) use a maximum luminosity spectrum to indisputably classify SN 2022joj as a SN Ia based on its blue color and persistent Si II features.

2.2. Host Galaxy

The host of SN 2022joj is a dwarf galaxy at $\alpha_{\text{J2000}} = 14^{\text{h}}41^{\text{m}}40^{\text{s}}.04$, $\delta_{\text{J2000}} = +03^{\circ}00'24''.53$, cataloged in the DESI Legacy Survey (LS; Dey et al. 2019), and has a g -band magnitude of 22.1 mag. SN 2022joj has a projected offset of only $0''.5 \pm 0''.1$ to the host. To measure the redshift of the host, we obtained two spectra about 1 year after the maximum brightness. On 2023 March 14, we took a spectrum of both the SN and the host using Binospec (Fabricant et al. 2019) on the 6.5m MMT telescope with a total integration time of 5400 s. We placed the slit across both the center of the galaxy and the position of the SN (Figure 3). On 2023 April 26, we took another spectrum using the Low Resolution Imaging Spectrometer (LRIS; Oke et al. 1995) on the Keck I 10m telescope. The slit was placed at the same position angle, with the Cassegrain Atmospheric Dispersion Compensator (Cass ADC; Phillips et al. 2006) module on. The total integration time was 3600 s. Both spectra were reduced with the PyPeIt package (Prochaska et al. 2020). The LRIS spectrum has a higher signal-to-noise ratio (S/N), in which we detected a potential host emission line at 6742.4 \AA (see Figure 3) with a S/N^1 of 3.2 while the continuum spectrum of the host was still outshined by the SN. If this is associated with the $\text{H}\alpha$ emission, the corresponding redshift of the host galaxy is $z = 0.02736 \pm 0.0007$, which is in general agreement with the estimated value $z = 0.03$ by matching the SN spectra to SNID templates (Newsome et al. 2022). In the coadded 2D spectrum, the trace is dominated by the light of the SN in the nebular phase, while the center of this emission feature has a offset of $\sim 3\text{--}4$ pixels to the center of the trace. The CCDs equipped on LRIS have a pixel scale of $0''.135/\text{pixel}$, so this offset corresponds to an angular offset of $\sim 0''.4\text{--}0''.5$, consistent with the archival value. The Binospec spectrum has a lower S/N, and we unambiguously identify this emission line at the same position in the 2D spectrum via visual inspection. Nevertheless, we still detect an emission feature in the

¹ We fit the emission line with a Gaussian profile to estimate its intensity, and the S/N is defined as the intensity divided by its uncertainty.

1D spectrum with a S/N of 1.6 at the same wavelength. All the evidence indicates that the H α detection is real.

We estimate the distance modulus of SN 2022joj in the following way. We first use the 2M++ model (Carriker et al. 2015) to estimate the peculiar velocity of the host galaxy to be $383 \pm 250 \text{ km s}^{-1}$. Then the peculiar velocity is combined with the recession velocity in the frame of the cosmic microwave background (CMB) $v_{\text{CMB}} = 8424 \text{ km s}^{-1}$, which yields a net Hubble recession rate of $8193 \pm 250 \text{ km s}^{-1}$. Using cosmological parameters $H_0 = 70 \text{ km s}^{-1} \text{ Mpc}^{-1}$, $\Omega_M = 0.3$, and $\Omega_\Lambda = 0.7$, the estimated luminosity distance to SN 2022joj is 119.5 Mpc, equivalent to a distance modulus of $35.39 \pm 0.03 \text{ mag}$.

2.3. Optical Photometry

SN 2022joj was monitored in g_{ZTF} , r_{ZTF} , and i_{ZTF} by ZTF as part of its ongoing Northern Sky Survey (Bellm et al. 2019b). The i_{ZTF} data only cover the decline from the peak. We use the forced-photometry light curves from ZFPS, reduced using the pipeline from A. A. Miller et al. (2023, in preparation); see also Yao et al. (2019). We adopt a Galactic extinction of $E(B - V)_{\text{MW}} = 0.032 \text{ mag}$ (Schlafly & Finkbeiner 2011), and correct all photometry using the extinction model from Fitzpatrick (1999) assuming $R_V = 3.1$. We do not find any Na I D absorption at the redshift of the host galaxy, indicating that the extinction from the host is negligible. The blue $g_{\text{ZTF}} - r_{\text{ZTF}}$ color ($\sim -0.2 \text{ mag}$) near maximum luminosity after correcting for the Galactic extinction is also consistent with no additional reddening from the host. Therefore we assume $E(B - V)_{\text{host}} = 0$. The dereddened g_{ZTF} and r_{ZTF} forced-photometry light curves in absolute magnitudes are shown in Figure 1.

[AAM: We include observations for LT and KAIT in a table (updated reduction) – less than 5 epochs, good ZTF coverage – exclude from analysis]

2.4. Swift Ultraviolet/Optical Telescope (UVOT) Observations

UV observations of SN 2022joj were obtained using the UVOT (Roming et al. 2005) mounted on the Gehrels Swift Observatory (Swift; Gehrels et al. 2004) following a time-of-opportunity (ToO) request. [AAM: who submitted the TOO?] Pre-SN reference images are only available in u , $uvw1$, and $uvw2$ filters. In all three bands the flux is consistent with 0, and all the $3\text{-}\sigma$ upper limits are $\lesssim 10\%$ of the corresponding UV flux measured after the onset of SN 2022joj. In the optical bands, the LS photometry ($g = 22.1 \text{ mag}$) shows that the host galaxy contributes $\lesssim 1\%$ of the total observed flux. We there-

fore conclude that the host galaxy can be neglected in estimating the SN flux.

We estimate the flux in the u , b , v , $uvw1$, $uvm2$, and $uvw2$ filters using a $5''$ circular aperture centered at the position of the SN. To estimate the brightness of the sky background we use a coaxial annulus region with an inner/outer radius of $8''/10''$. The reduction is performed with the package HEASoft² (HEASARC 2014).

2.5. Optical Spectroscopy

We obtained a series of optical spectra of SN 2022joj using the Spectral Energy Distribution Machine (SEDm; Blagorodnova et al. 2018) on the automated 60 inch telescope (P60; Cenko et al. 2006) at Palomar observatory, the Andalucia Faint Object Spectrograph and Camera (ALFOSC)³ installed at the Nordic Optical Telescope (NOT), the SPectrograph for the Rapid Acquisition of Transients (SPRAT; Piascik et al. 2014) on the 2 m Liverpool Telescope (LT; Steele et al. 2004), FLOYDS spectrograph⁴ on the 2 m Faulkes Telescope South (FTS) at Siding Spring as part of the Las Cumbres Observatory global telescope (LCOGT) network (Brown et al. 2013), Binospec on the 6.5 m MMT telescope, and LRIS on the Keck I 10 m telescope. With the exception of observations obtained with SEDm, all spectra were reduced using standard procedures (e.g., Matheson et al. 2000). The SEDm spectra were reduced using the custom pyse dm software package (Rigault et al. 2019). Details of the spectroscopic observations are listed in Table 1. The resulting spectral sequence is shown in Figure 2. All the spectra listed in Table 1 will be available on WISerEP (Yaron & Gal-Yam 2012).

We also include the spectrum uploaded to the Transient Name Server (TNS) by Newsome et al. (2022) in our analysis, which was obtained using the FLOYDS spectrograph on the 2 m Faulkes Telescope North (FTN) at Haleakala.

3. ANALYSIS

3.1. Early Light Curves and the First Light

To estimate the time of first light (t_{fl}), we assume an initial power-law rise in the broad-band flux $f(t)$,

$$f(t) = A(t - t_{\text{fl}})^\alpha,$$

where A is a constant and α is the power-law index. We only include the forced-photometry light curve with

² <http://heasarc.gsfc.nasa.gov/ftools>

³ <http://www.not.iac.es/instruments/alfosc/>

⁴ <https://lco.global/observatory/instruments/floyds/>

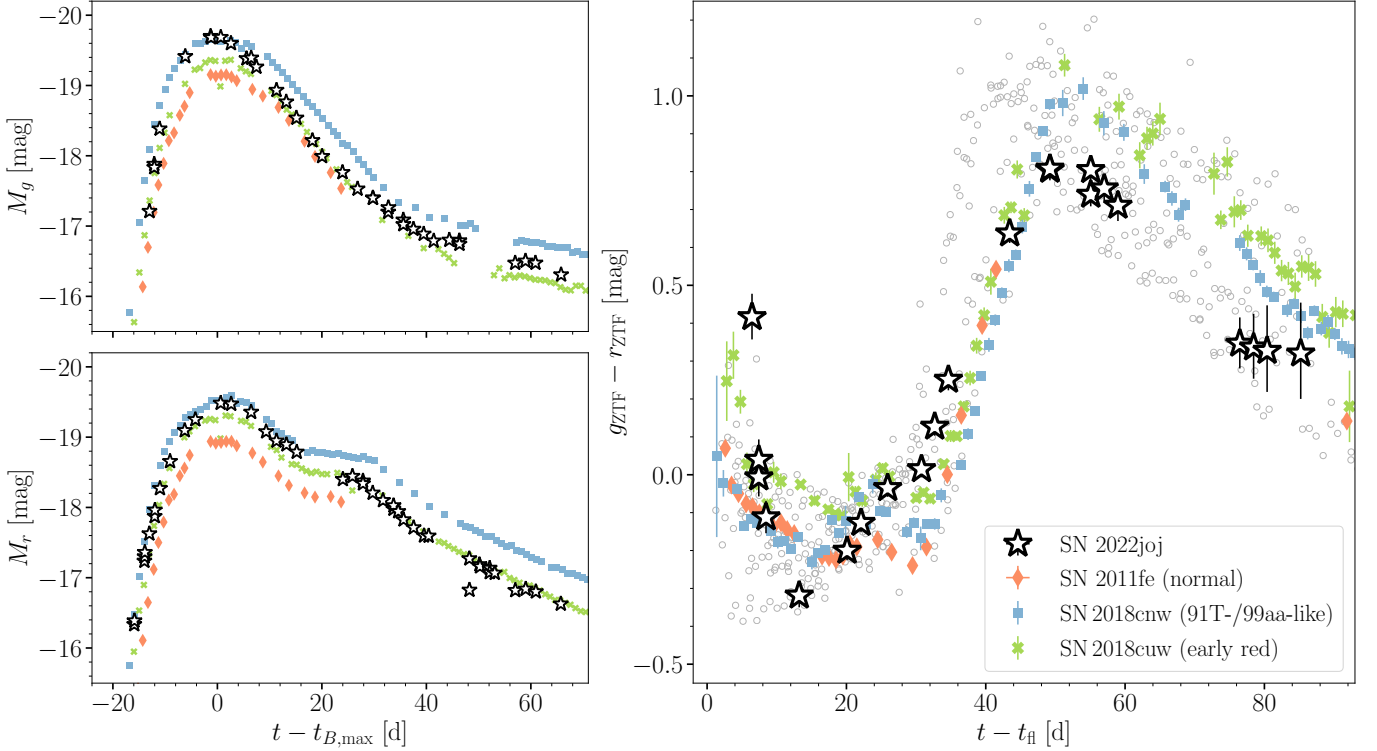


Figure 1. Comparison of the photometric properties of SN 2022joj with SN 2011fe (normal Ia; [Pereira et al. 2013](#)), SN 2018cnw (91T-/99aa-like), and SN 2018cuw (normal Ia with a red early color). *Left*: multiband light curves. The upper (lower) panel shows the evolution in the g -band (r -band) absolute magnitude. *Right*: $g_{ZTF} - r_{ZTF}$ color evolution. The gray circles denote the color evolution of 14 nearby ($z \leq 0.05$) SNe Ia (open circles) from the ZTF sample with prompt observations within 5 days of first light ([Bulla et al. 2020](#)). Note that K -corrections have not been applied.

Table 1. Spectroscopic observations of SN 2022joj.

t_{obs}	Phase	Telescope/	R	Range
(MJD)	(days)	Instrument	($\lambda/\Delta\lambda$)	(\AA)
59,710.29	-12.1	FTN/FLOYDS-N	550	3500–10000
59,725.34	+2.5	P60/SEDm	100	3770–9220
59,725.43	+2.6	P60/SEDm	100	3770–9220
59,732.02	+9.0	NOT/ALFOSC	360	3500–9700
59,744.96	+21.6	LT/SPRAT	350	4020–7990
59,752.50	+29.0	FTS/FLOYDS-S	550	3500–10000
59,759.92	+36.2	LT/SPRAT	350	4020–7990
59,760.37	+36.6	Keck I/LRIS	1100	3100–10280
59,784.89	+60.5	NOT/ALFOSC	360	3850–9620
60,017.42	+286.8	MMT/Binospec	1340	3830–9210
60,061.56	+329.8	Keck I/LRIS	1100	3200–10150

NOTE—Phase is measured relative to the B -band peak in the rest frame of the host galaxy. The resolution R is reported for the central region of the spectrum.

flux $\leq 40\%$ of peak luminosity ([Miller et al. 2020](#)) in r_{ZTF} and ATLAS o , in which observations were conducted on more than three nights between -20 days and -10 days. Light curves in other bands are excluded because the coverage is significantly worse at this phase

(see Section 3.2). We assume that the t_H is the same in both bands, then estimate α and $\ln A$ in each band with a Bayesian approach. We adopt flat priors for t_H and $\log A$, and a normal prior for each α centered at 2 (the fireball model) with a standard deviation of 1. We sample their posterior distributions with Markov Chain Monte Carlo (MCMC) using the package PyMC ([Salvatier et al. 2016](#)). In addition, we run another model with a fixed $\alpha = 2$. The estimated model parameters are listed in Table 2. We find that both light curves are consistent with a power-law rise, in which the first detection in r_{ZTF} is $4.16^{+0.58}_{-0.70}$ days after the first light. This estimate is consistent with the $\alpha = 2$ fireball model. When fixing $\alpha = 2$, the model also fits the light curve well, but the estimated t_H is ~ 0.5 day later. We do not find any correlated residuals as evidence for a flux excess after ~ 4 days since t_H , although a flux excess before the first detection could not be ruled out.

3.2. Photometric Properties

The basic photometric properties of SN 2022joj are listed in Table 2. The times of the maximum luminosity and the corresponding magnitudes in the ZTF g and r bands are estimated both in a fourth-order polyno-

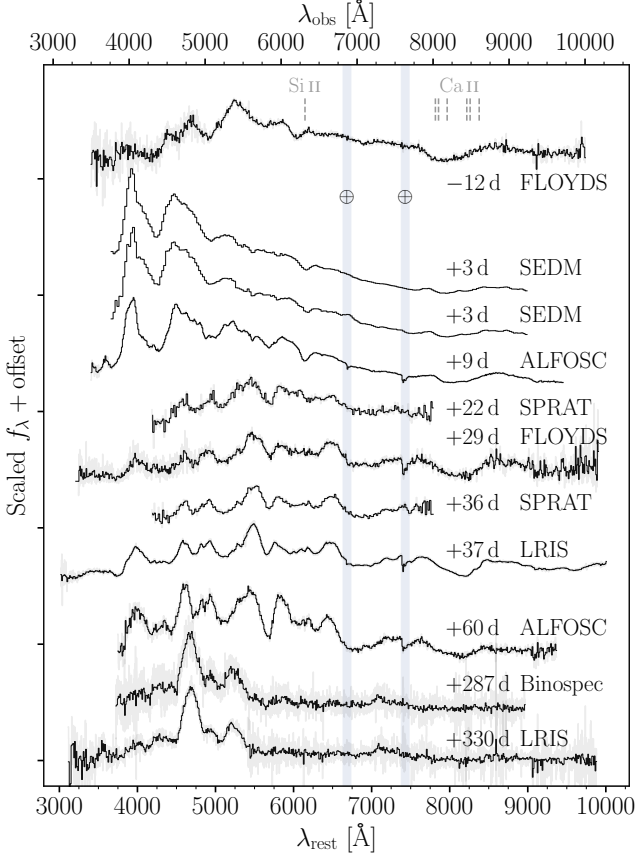


Figure 2. Optical spectral sequence of SN 2022joj shows the red to blue color transition as the SN rises to its maximum luminosity and the development of prominent absorption features around 4300 Å afterward. Rest-frame phase relative to the B -band peak and the instrument used are listed next to each spectrum. Spectra have been corrected for $E(B - V)_{\text{MW}} = 0.032$ mag and are shown in gray. The black lines are binned spectra with a bin size of 10 Å, except for the SEDM spectra, whose resolution is lower than the bin size. The corresponding wavelengths of the Si II $\lambda 6355$ line (with an expansion velocity of 10,000 km s⁻¹) and the Ca II IRT (with expansion velocities of both 10,000 km s⁻¹ and 25,000 km s⁻¹) are marked by the vertical dashed lines. The strong optical telluric features (Fraunhofer A and B bands) are marked by the shaded region.

mial fit. We do not include the maximum i_{ZTF} -band properties, which are relatively uncertain due to the low cadence in i_{ZTF} around peak. In addition, we feed the UVOT b and v , ZTF g , r , and i , as well as ATLAS o light curves simultaneously to the SALT3 (Kenworthy et al. 2021) model with the package `sncosmo` (Barbary et al. 2023), which enable us to estimate the Bessell B -band properties. However, we find that the SALT3 model cannot reproduce the broadband colors at maximum luminosity. It underestimates the maximum brightness in r_{ZTF} . The predicted M_{max} in r_{ZTF} are 0.08 mag ($\sim 15\sigma$)

fainter than the highest observed flux. Meanwhile, it overestimates the maximum brightness in UVOT b by 0.18 mag ($\sim 6\sigma$). This indicates that SN 2022joj is a peculiar event, and we thus do not trust the t_{max} and M_{max} provided in the SALT3 fit. Instead, we adopt the epoch (MJD 59722.75) and the magnitude (-19.62 ± 0.03 mag) of the last Swift observation in UVOT b as the t_{max} and M_{max} in Bessell B .⁵

SN 2022joj shows a few peculiar photometric features compared to normal SNe Ia. In Figure 1, we compare the g_{ZTF} and r_{ZTF} light curves and the $g_{\text{ZTF}} - r_{\text{ZTF}}$ color evolution of SN 2022joj with those of the well-observed normal SN Ia, SN 2011fe,⁶ as well as SN 2018cnw (ZTF18abauprj) and SN 2018cuw (ZTF18abcflnz) from a sample of SNe Ia with prompt observations within 5 days of first light by ZTF (Yao et al. 2019; Bulla et al. 2020). SN 2018cnw is slightly overluminous at peak, and belongs to either the SN 1999aa-like (99aa-like; Garavini et al. 2004) or SN 1991T-like (91T-like; Filippenko et al. 1992a) subclass of SNe Ia, while SN 2018cuw is a normal SN Ia with a red $g_{\text{ZTF}} - r_{\text{ZTF}}$ color comparable to that of SN 2022joj ~ 15 days prior to peak.

Around maximum brightness, SN 2022joj is overluminous, comparable to SN 2018cnw, and ~ 0.5 mag brighter than SN 2011fe in both g_{ZTF} and r_{ZTF} . But SN 2022joj clearly stands out due to its fast evolution in g_{ZTF} . While SN 2022joj and SN 2018cnw show a similar maximum brightness in g_{ZTF} , upon the first detection of SN 2022joj in g_{ZTF} at ~ -13 days, its corresponding absolute magnitude (-17.2 mag) is ~ 0.8 mag fainter than that of SN 2018cnw at a similar phase. This means on average, SN 2022joj rises faster than SN 2018cnw by ~ 0.06 mag day⁻¹ in g_{ZTF} during that period of time. On the decline, the $\Delta m_{15}(g_{\text{ZTF}})$ of SN 2022joj is 1.03 ± 0.03 mag, which is significantly greater than that of the overluminous SN 2018cnw ($\Delta m_{15}(g_{\text{ZTF}}) = 0.77$ mag) or normal SN 2011fe ($\Delta m_{15}(g_{\text{ZTF}}) = 0.80$ mag) [Chang: for all of these the coverage is good so you can fit a polynomial and provide uncertainties][AAM: Both show uncertainty much smaller than 0.01 mag]. This is atypical for overluminous SNe Ia, which are among the slowest decliners in the SN Ia population (Phillips et al. 1999; Taubenberger 2017). [AAM: SNe evolve apparently slower at higher redshifts, so a slow-decliner can be a normal event whose redshift is underestimated –

⁵ There are known color terms in the transformation between UVOT b and Bessell B (Poole et al. 2008). For the $b - v \simeq 0$, as is observed in SN 2022joj around maximum brightness, $B - b$ is of the order of 0.02 mag.

⁶ We show the synthetic photometry in g_{ZTF} and r_{ZTF} calculated using the spectrophotometric sequence from Pereira et al. (2013).

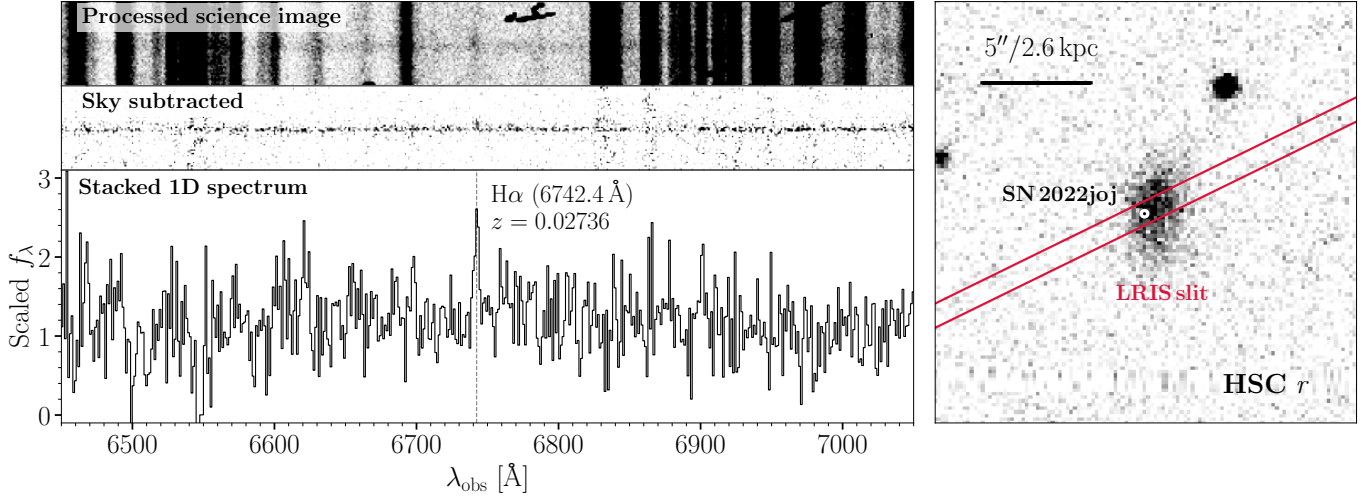


Figure 3. The LRIS spectrum reveals an $H\alpha$ emission line from the host galaxy at 6742.4 \AA , corresponding to a redshift $z = 0.02736$. *Left:* the $H\alpha$ emission in the observed 2D and 1D spectrum. This emission line sits in the region free of strong sky lines and is unlikely due to bad sky subtraction. *Right:* image of SN 2022joj and its host galaxy with the orientation of the LRIS slit overplotted.

however, fast-decliners are intrinsically fast-decliners.] The rapid decline is probably due to the unusual and fast-developing absorption feature near 4200 \AA (see Section 3.3). In r_{ZTF} SN 2022joj evolves similar to other SNe Ia, although the evolution still appears slightly faster.

The color evolution of SN 2022joj does not match normal SNe Ia, as shown by the trail traced by SN 2022joj in the right panel of Figure 1. We overplot all the SNe from the ZTF early Ia sample (Bulla et al. 2020) with a redshift $z \leq 0.05$. They are corrected for Galactic extinction, but K -corrections have not been performed for consistency. Given the peculiar nature of SN 2022joj, we cannot use models trained on normal SNe Ia to reliably estimate its K -correction. Nevertheless, given its relatively low redshift ($z \lesssim 0.03$), the K -correction is not expected to be large. For the same reason we only include the SNe Ia with the lowest redshift from the sample of Bulla et al. (2020). SN 2022joj is remarkably red ($g_{\text{ZTF}} - r_{\text{ZTF}} \simeq 0.4 \text{ mag}$) around ~ 7 days after t_{B} , and is clearly an outlier compared to the normal Ia sample.⁷ During the ensuing week, SN 2022joj quickly evolves to the blue, and is among the bluest objects in the sample ~ 15 days after t_{B} . SN 2018cuw has a comparable $g_{\text{ZTF}} - r_{\text{ZTF}}$ color at early times, but the blueward evolution of SN 2018cuw is slower than SN 2022joj. From ~ 10 – 20 days after t_{B} , before it reaches

maximum brightness, SN 2022joj starts to evolve redward in the next ~ 2 months. While other SNe Ia show qualitatively similar behavior, this redward evolution usually begins at a much later phase, ~ 30 days after t_{B} . When $g_{\text{ZTF}} - r_{\text{ZTF}}$ reaches maximum ($\sim 0.8 \text{ mag}$) ~ 50 days after t_{B} , SN 2022joj is again bluer than most of the SNe Ia in the ZTF sample. Eventually as SN 2022joj steps into the transitional phase, its color evolution follows the Lira law⁸ (Lira 1996; Phillips et al. 1999) and shows no significant difference from that of SNe Ia.

While SN 2022joj shows a blue $g_{\text{ZTF}} - r_{\text{ZTF}}$ color near maximum, its near-UV colors are unusually red. After correcting for Galactic extinction, SN 2022joj shows $u - v = 1.59 \pm 0.06 \text{ mag}$ and $uvw1 - v = 3.99 \pm 0.21 \text{ mag}$. In a sample of 29 normal SNe Ia with UV observations around maximum from Brown et al. (2018), however, none of the objects shows $u - v > 0.5 \text{ mag}$ or $uvw1 - v > 2.1 \text{ mag}$. If we compare SN 2022joj ($b - v = -0.09 \pm 0.06 \text{ mag}$ at peak) only to the 8 “optically-blue” ($b - v \leq 0$ at peak) objects in the sample, we find that these “optically-blue” objects tend to show even bluer near-UV colors ($u - v \lesssim -0.3 \text{ mag}$, $uvw1 - v \lesssim 1.5 \text{ mag}$). Interestingly, SN 2022joj shows a moderately blue mid-UV color ($uvm2 - uvw1 = 1.52 \pm 0.40 \text{ mag}$) compared to normal SNe Ia, most of which show $uvm2 - uvw1 \gtrsim 2 \text{ mag}$. This might indicate that, for some reason, the flux in near-UV (~ 2500 – 4000 \AA) of SN 2022joj is suppressed near maximum brightness.

⁷ There is one point close to the first detection of SN 2022joj in the color evolution diagram, which belongs to SN 2018dhw (ZTF18abfhyrc). This single $g_{\text{ZTF}} - r_{\text{ZTF}}$ measurement has an uncertainty of $\sim 0.1 \text{ mag}$ and is $2\text{-}\sigma$ redder than measurements made the night before and after.

⁸ The original Lira law was discovered in $B - V$ color. But in the $g_{\text{ZTF}} - r_{\text{ZTF}}$ color we see a similar trend.

To conclude, despite a similar luminosity and color to 99aa-like/91T-like events at maximum brightness, the rapid photometric rise and decline and the unusual color evolution in SN 2022joj both indicate that it exhibits some peculiarities relative to normal SNe Ia.

3.3. Optical Spectral Properties

In Figure 2, we show the optical spectral sequence of SN 2022joj. The -12 days spectrum exhibits prominent absorption lines associated with Si II $\lambda 6355$ and Ca II IRT (this spectrum was obtained and posted on TNS by Newsome et al. 2022). It also shows a strong suppression of flux blueward of ~ 5000 Å, confirming the unusually red photometric colors at early times. Near maximum brightness, the two SEDM spectra show a very blue continuum between ~ 5000 – 8000 Å with shallow absorption features, indicating a high photometric temperature. Si II $\lambda\lambda 5972$, 6355 lines, the S II W-trough, and Ca II IRT are detectable but not prominent. A wide, asymmetric absorption feature appears between ~ 4000 – 4500 Å (the 4200 Å features hereafter). There is a break on the blue edge of this feature which could be associated with Si II $\lambda 4128$ that is widely seen in other SNe Ia. However, the spectra of most normal and overluminous 99aa-like/91T-like SNe Ia show another peak at ~ 4100 – 4200 Å redward of a narrow Si II $\lambda 4128$ feature, which is absent in the spectra of SN 2022joj (see the left panel of Figure 4). The 4200 Å features become even wider and deeper in the ALFOSC spectrum at $\sim +9$ days. Weeks after the maximum, in the FLOYDS spectrum ($+29$ days) and the LRIS spectrum ($+36$ days), the bottom of the 4200 Å features becomes flat, reminiscent of the Ti-trough in the subluminal SN 1991bg-like (91bg-like; Filippenko et al. 1992b; Leibundgut et al. 1993). The nebular-phase spectra are dominated by [Fe II], [Fe III], and [Co III] emission lines, but the [Fe II] features (e.g., the complex around ~ 7300 Å) are weaker than in other SNe Ia, suggesting that the ejecta remain highly ionized. The nebular spectra are discussed in detail in Section 4.2.

In Figure 4, we compare maximum light and transition phase spectra of SN 2022joj to other SNe Ia. Around peak, the blue continuum and shallow absorption features in SN 2022joj are similar to overluminous objects, including SN 1991T, SN 1999aa, and SN 2000cx. The asymmetric 4200 Å features are not seen in SN 1991T or SN 1999aa, while in SN 2000cx, a similar (but narrower) absorption feature is interpreted as high velocity Ti II (Branch et al. 2004). The 4200 Å features are actually much more similar to the well-known Ti-

trough that is ubiquitous in subluminal 91bg-like objects, e.g., SN 1999by (Arbour et al. 1999). Prior to the peak, SN 1999by also shows this asymmetric absorption at about the same wavelength. In 91bg-like SNe, this absorption feature becomes more prominent with a nearly flat-bottom trough about a week after maximum. This absorption is caused by a blend of multiple IGEs dominated by Ti II (Filippenko et al. 1992b; Mazzali et al. 1997). It remains prominent in the spectrum up to one month after maximum. Similarly, we find that this trough is prominent in the spectra of SN 2022joj at $+29$ days and $+36$ days. Other normal/overluminous SNe Ia, unlike SN 2022joj, all exhibit a dip around ~ 4500 Å. Aside from the 4200 Å features, SN 2022joj is otherwise entirely dissimilar to 91bg-like objects, which are $\gtrsim 2$ mag fainter at peak and exhibit much stronger Si II, Ca II and O I absorption from a cooler line-forming region (Filippenko et al. 1992b). The Ti-trough in 91bg-like SNe is interpreted as the result of a low photospheric temperature (Mazzali et al. 1997). Whether the 4200 Å features in SN 2022joj are dominated by Ti II absorption is unclear.

SN 2022joj also shows remarkably shallow Si II absorption at maximum brightness. Following the techniques elaborated in Liu et al. (2023a) (see also Childress et al. 2013, 2014; Maguire et al. 2014), we fit the Si II and Ca II IRT features with multiple Gaussian profiles. We find that the modeling Ca II IRT absorption requires two distinct velocity components – the photospheric velocity features (PVFs) and the high velocity features (HVs). In Table 3 we list the estimates of the expansion velocities and the pseudo-equivalent widths (pEW s) of the major absorption lines from ~ -12 days to $\sim +9$ days. In Figure 5 we show the peak absolute magnitude in B band vs. the velocity and pEW of Si II for SN 2022joj and a sample of normal SNe Ia from Zheng et al. (2018) and Burrow et al. (2020). Figure 5 highlights that SN 2022joj is slightly overluminous with a relatively low Si II $\lambda 6355$ expansion velocity (hereafter $v_{Si II}$). The Si II $\lambda 5972$ and Si II $\lambda 6355$ pEW s in SN 2022joj are lower than most normal SNe Ia. In fact, SN 2022joj sits at the extreme edge of the shallow-silicon group proposed in Branch et al. (2006), which mainly consists of overluminous 91T-like/99aa-like objects. This is consistent with the high luminosity and the blue color of SN 2022joj at maximum light, since a high photometric temperature results in higher ionization, reducing the abundance of singly ionized atoms (e.g., Si II). Interestingly, the pEW of Si II $\lambda 6355$ near peak is significantly lower than that in the first spectrum. In typical 91T-like/99aa-like objects, the Si II features are weak or undetectable at early times because the ejecta are even hotter, and only start to emerge

Table 2. Basic photometric properties of SN 2022joj.

Rise (flux $\leq 40\%$ of peak luminosity)			
t_{fl} (MJD)	$59703.16^{+0.70}_{-0.58}$		
$\alpha_{\text{ZTF},r}$	$2.18^{+0.20}_{-0.24}$		
$\alpha_{\text{ATLAS},o}$	$2.37^{+0.48}_{-0.20}$		
$t_{\text{fl},\alpha=2}$ (MJD)	$59703.66^{+0.10}_{-0.11}$		
Maximum luminosity			
Filters	g_{ZTF}	r_{ZTF}	B
$t_{\text{max,poly}}$ (MJD)	59722.65 ± 0.22	59725.13 ± 0.08	\dots
$M_{\text{max,poly}}$ (mag)	-19.693 ± 0.013	-19.489 ± 0.004	\dots
$t_{\text{max,SALT}}$ (MJD)	59724.21 ± 0.03	59725.29 ± 0.03	59723.40 ± 0.03
$M_{\text{max,SALT}}$ (mag)	-19.677 ± 0.006	-19.407 ± 0.002	-19.802 ± 0.009

NOTE—The absolute magnitudes have been corrected for Galactic extinction.

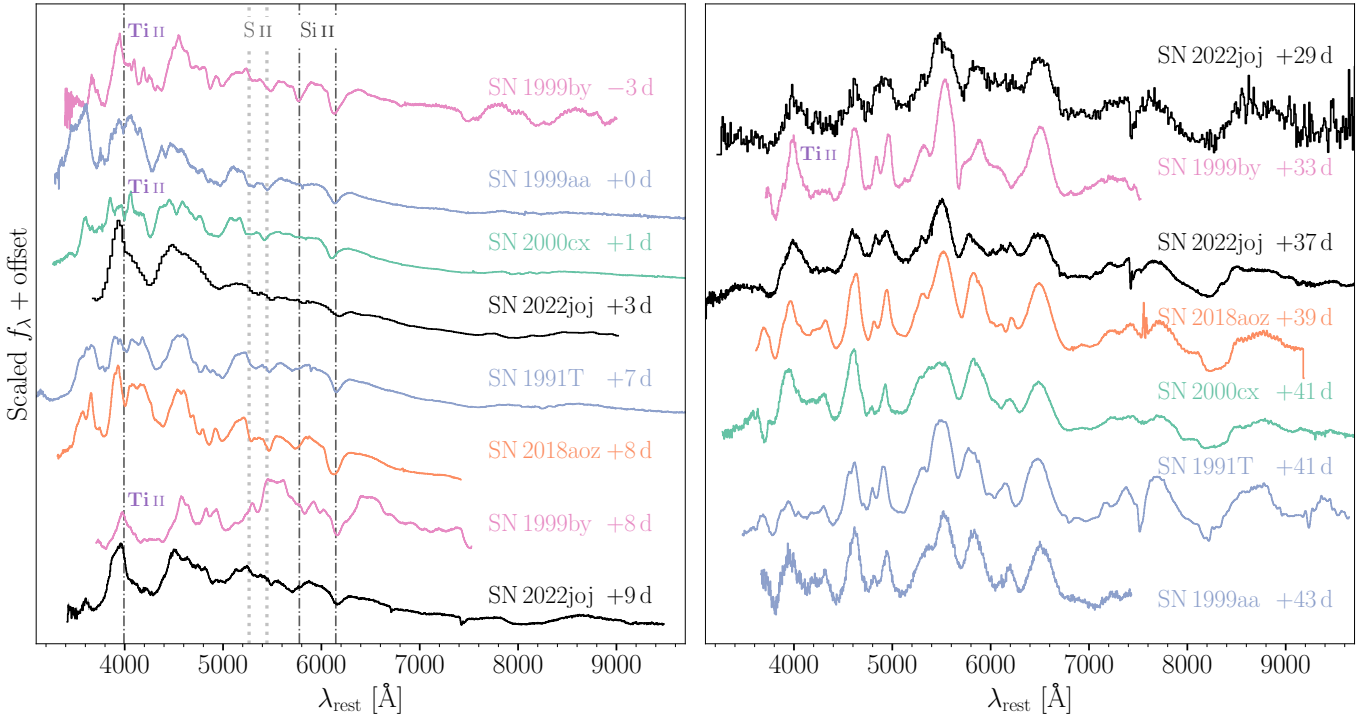


Figure 4. Optical spectra of SN 2022joj (black) and (i) a subluminous SNIa, SN 1999by (magenta), (ii) two overluminous SNIa, SN 1991T and SN 1999aa (blue), (iii) the peculiar SN 2000cx (green), and (iv) a normal SNIa with a red color at early times, SN 2018aoz (orange), near maximum brightness (left panel) and a month after maximum (right panel). The dash-dotted lines correspond to wavelengths of three Si II lines (4128 Å, 5972 Å, and 6355 Å), while the dotted lines correspond to the wavelengths of the S II W-trough (both assuming an expansion velocity of $10,000 \text{ km s}^{-1}$). Ti II has been identified from the spectra of SN 1999by and SN 2000cx at around ~ 4200 Å, and the corresponding features are labeled. Spectra were downloaded from WiseREP (Yaron & Gal-Yam 2012), with the following original data sources: SN 1991T, SN 1999aa, and SN 2000cx – Silverman et al. (2012); SN 1999by – Matheson et al. (2008); SN 2018aoz – Ni et al. (2023).

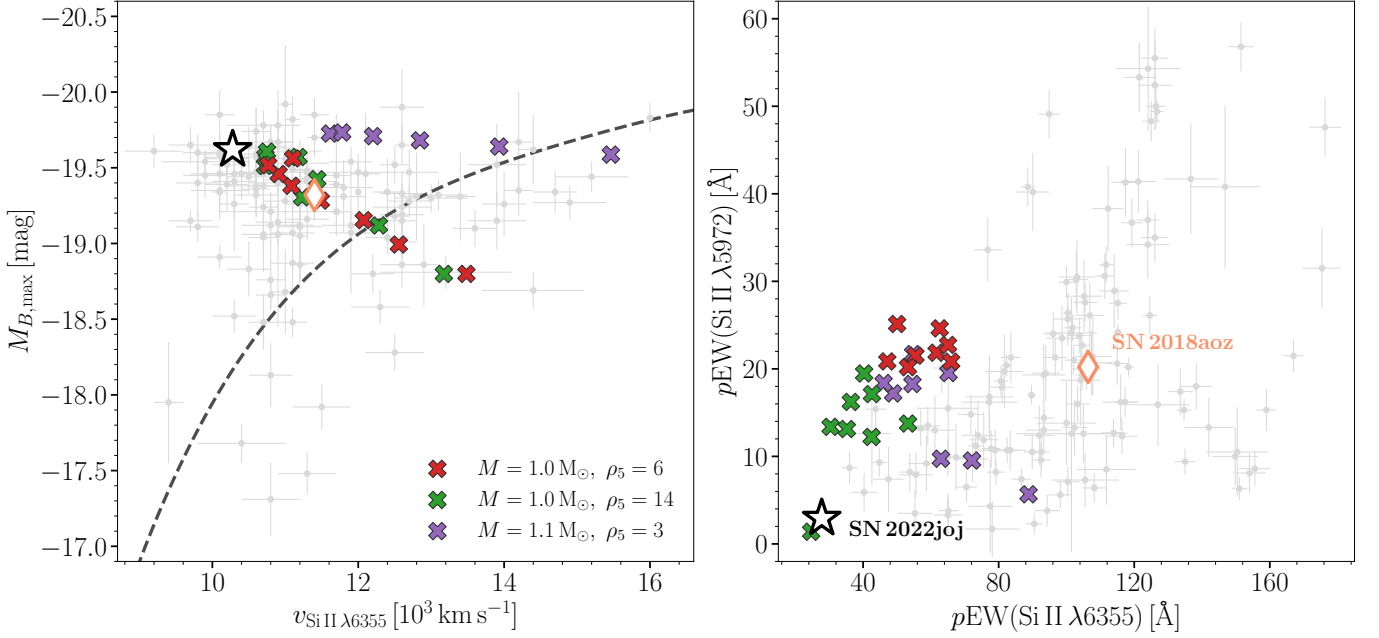


Figure 5. SN 2022joj (black star) as an overluminous SN Ia marked by its shallow Si II features. *Left:* the B -band absolute magnitude versus the expansion velocity of Si II $\lambda 6355$ at maximum brightness. *Right:* the pseudo-equivalent width ($p\text{EW}$) of the two Si II lines, Si II $\lambda\lambda 5972, 6355$, at maximum brightness. The grey dots show normal SNe Ia from Zheng et al. (2018) and Burrow et al. (2020). The dashed black line corresponds to the theoretical $M_{B,\text{max}}-v_{\text{Si II}}$ relation of 1D DDet models for thin helium shells across a spectrum of progenitor masses in Polin et al. (2019). The colored \times symbols show 2D DDet [Chang: I can't remember what we did in 20byg, but I thought we avoided DDet since it can also be interpreted as delayed detonation?] [AAM: I remember doing a quick search when writing the 20jgb paper, finding that delayed detonation is usually abbreviated as DD (which is a bummer as it can also be double degenerate)] models from Shen et al. (2021b) with different total masses (M), densities at the bottom of the helium shell (ρ_5 in units of 10^5 g cm^{-3}), and viewing angles (μ defined as the cosine of the polar angle relative to the point where the helium-shell detonation occurs). For each model, multiple symbols are shown to summarize the effect of different viewing angles, from $\mu = -0.93$ to $\mu = +0.93$. Parameters of the potential DDet normal SN Ia, SN 2018aoz (Ni et al. 2023), are also overplotted as an orange diamond.

around maximum light (Filippenko et al. 1992a). In the early spectrum of SN 2022joj, in contrast, stronger absorption features from singly ionized Si and Ca indicate a cooler line-forming region at early times compared to maximum brightness.

In conclusion, the spectral evolution of SN 2022joj shows some similarities to 91T-like/99aa-like objects, as well as peculiarities. A reasonable model to explain SN 2022joj needs to reproduce (i) a strong suppression in flux blueward of $\sim 5000 \text{ \AA}$ at early times followed by a rapid evolution to blue colors; (ii) the seemingly contradictory observables at peak, namely the tentative Ti II features and the blue continuum/shallow Si II feature at maximum, which separately indicate low and high photometric temperatures, respectively.

4. DISCUSSION

4.1. Models

[Chang: I think we should be more descriptive than just models for this section]

There are several physical mechanisms that can produce blue colors during the early evolution of SNe Ia, including: heating of the SN ejecta following the decay of radioactive ^{56}Ni , interaction of the SN ejecta with a nondegenerate companion (e.g., Kasen 2010), collisions between the SN ejecta and circumstellar material (e.g., Piro & Morozova 2016), strong mixing that surfaces ^{56}Ni to the outermost layers of the ejecta (e.g., Piro & Nakar 2013; Magee & Maguire 2020), and/or via the production of radioactive isotopes in the detonation of a helium shell on the surface of the exploding WD (e.g., Noebauer et al. 2017; Polin et al. 2019).

On the other hand, there are few proposed scenarios that can produce red colors up to a week after explosion, as is the case of SN 2022joj. If the newly synthesized ^{56}Ni is strongly confined to innermost SN ejecta, then a SN may remain red for several days after explosion as the heating diffuses out towards the photosphere (Piro & Morozova 2016). Even the most confined ^{56}Ni configuration considered in Piro & Morozova (2016) converges to blue colors, similar to explosions with more extended ^{56}Ni distributions, within ~ 6 days after explosion. SN 2022joj is observed to have very red colors ~ 7 days after t_{H} (meaning more than 7 days after explosion, since SNe Ia have a “dark phase” before photons diffuse out of the ejecta; Piro & Nakar 2013). Dessart et al. (2014) considered more realistic delayed-detonation scenario. Some of their 1D unmixed delayed-detonation models still show a red $B - R$ color ($B - R \gtrsim 0.5 \text{ mag}$) 7 days after the explosion (see

the DDC20, DDC22, and DDC25 models in their Figure 1). However, these models never appear as blue as SN 2022joj, and the ^{56}Ni yields are relatively low ($m_{\text{Ni}56} \lesssim 0.3 M_{\odot}$), so they would result in subluminal events. In addition, we do not know any multidimensional explosion models that fail to produce any ^{56}Ni mixing within the ejecta, and therefore disfavor this scenario.

Alternatively, in the DDet scenario, a layer of IGEs in the ashes of the helium shell can produce significant opacity in the outer layers of the bulk ejecta, producing a red color (Polin et al. 2019). This scenario has been proposed for a few SNe with red colors at early times, including SN 2016jhr (Jiang et al. 2017) and SN 2018aoz (Ni et al. 2022). In Figure 6 we compare the spectra of SN 2022joj at ~ -12 days and near maximum light with 1D DDet models from Polin et al. (2019) and 2D DDet models from Shen et al. (2021b). To create synthetic spectra, both models use Sedona, multi-dimensional radiative transfer (RT) simulator that assumes local thermodynamical equilibrium (LTE).

In the 1D models, the most important model parameters are the mass of the C/O core (M_c) and the mass of the helium shell (M_s). The maximum luminosity depends on the amount of ^{56}Ni synthesized in the explosion, which is predominantly determined by the total progenitor mass ($M_c + M_s$) in 1D models (Polin et al. 2019). We find that the maximum brightness in B band ($M_{B,\text{max}} = -19.82 \text{ mag}$) is reproduced by the 1D models with relatively massive progenitors ($\sim 1.2 M_{\odot}$). However, models with such massive progenitors tend to produce blue, featureless spectra at early times (e.g., the $M_c = 1.1 M_{\odot}$, $M_s = 0.05 M_{\odot}$ model in Figure 6), inconsistent with the observations. Less massive models provide a better match to the line-blanketing seen in the early spectra, but fail to reproduce the maximum brightness as well as the 4200 \AA features in the observed spectra. The 1D models overestimate the $p\text{EW}$ and the expansion velocity of the Si II $\lambda 6355$ line at peak. As a reference, we overplot the theoretical $M_{B,\text{max}} - v_{\text{Si II}}$ relation of 1D DDet models for thin helium shells across a spectrum of progenitor masses in Polin et al. (2019) as the dashed black curve in the left panel of Figure 5, which is not in agreement with the properties of SN 2022joj. [Chang: A couple more details are needed here - is that sequence for high mass shells? low mass shells? it does not capture every single model in Abi’s paper.] [AAM: Only thin shells - I don’t think Abi explicitly mentioned the mass of the shells though.]

While the 1D models do not fully reproduce the observed properties of SN 2022joj, some of these tensions can be resolved when considering viewing angle effects

Table 3. Fits to the expansion velocities and pEWs of Si II $\lambda\lambda 5972$, 6355 and the Ca II IRT of SN 2022joj.

Phase	Si II $\lambda 5972$		Si II $\lambda 6355$		Ca II IRT, PVFs		Ca II IRT, HVFs	
	v	pEW	v	pEW	v	pEW	v	pEW
(day)	(10^3 km s^{-1})	(Å)	(10^3 km s^{-1})	(Å)	(10^3 km s^{-1})	(Å)	(10^3 km s^{-1})	(Å)
−12.1	-15.66 ± 0.13	47.5 ± 2.5	-14.85 ± 0.83	190 ± 34	-25.98 ± 0.56	278 ± 40
+2.5	-8.77 ± 0.63	2.9 ± 1.5	-10.28 ± 0.13	27.8 ± 1.3	-12.03 ± 0.73	58 ± 11	-22.51 ± 0.33	109 ± 11
+2.6	-8.35 ± 0.62	4.4 ± 2.6	-9.87 ± 0.28	25.4 ± 2.7	-11.77 ± 0.93	85 ± 17	-22.17 ± 0.47	105 ± 15
+9.0	-10.37 ± 0.04	48.5 ± 0.6	-12.07 ± 0.25	147 ± 7	-21.21 ± 0.16	124 ± 7

in multi-dimensional models. In Figure 5 we also show the properties of three 2D DDet models from Shen et al. (2021b). The selected models have different total progenitor masses M and densities at the bottom of the helium shell ρ_5 (in units of 10^5 g cm^{-3}). For these models, we obtain the Si II line properties using the same fitting techniques as in Section 3.3. We again find that more massive progenitors generally lead to more luminous SNe, but different viewing angles produce significantly different spectral properties. In the plot, the cosine value of the polar angle relative to the point of helium detonation, μ , ranges from +0.93 (near the helium detonation) to −0.93 (opposite to the helium detonation). When the SN is observed along a line of sight closer to the detonation point in the shell (greater μ), it will appear fainter at maximum brightness and show a higher line velocity in Si II $\lambda 6355$. For a relatively high progenitor mass ($\gtrsim 1.1 M_\odot$), a high $v_{\text{Si II}}$ ($\gtrsim 13,500 \text{ km s}^{-1}$) is predicted. However, with $\mu \lesssim 0$, all the 2D models show a lower $v_{\text{Si II}}$ ($\lesssim 12,000 \text{ km s}^{-1}$), much closer to SN 2022joj in the $M_{B,\text{max}}-v_{\text{Si II}}$ phase space. Models with $\mu > 0$ are more consistent with 1D model predictions. It is argued in (Polin et al. 2019) that high-velocity SNe that follow the dashed line in Figure 5 are sub- M_{Ch} DDets, while SNe in the clump centered at $M_{B,\text{max}} \simeq -19.5 \text{ mag}$ and $v_{\text{Si II}} \simeq 11,000 \text{ km s}^{-1}$ are likely near- M_{Ch} explosions. Based on the 2D models, however, we should expect a similar number of high-velocity and normal-velocity DDet SNe Ia. A substantial fraction of the objects within the clump on the $M_{B,\text{max}}-v_{\text{Si II}}$ diagram may be sub- M_{Ch} DDet events viewed from certain orientations (Shen et al. 2021b). SN 2018aoz is a DDet candidate that, like SN 2022joj, exhibits early red colors before evolving to normal luminosity and blue colors (Ni et al. 2022). Interestingly, SN 2018aoz also resides in the high-luminosity, low-velocity clump in the $M_{B,\text{max}}-v_{\text{Si II}}$ space (Ni et al. 2023), and thus, it too may be an example of a DDet SNIa viewed from the opposite hemisphere opposite from helium detonation.

In the bottom panels of Figure 6 we show three 2D DDet models with a total progenitor mass of $\sim 1 M_\odot$ from Shen et al. (2021b). These models, particularly the $\mu = -0.67$ ones, qualitatively match the observed spectra at maximum light. The $\rho_5 = 6$ model has a helium shell of $\sim 0.05 M_\odot$. We find that when $\mu = 0$ (viewed from the equator), the model predicts a reasonable level of line blanketing in the blue side of the spectrum at early times (lower left panel of Figure 6). Near maximum brightness, the model also reproduces the overall shape of the observed spectrum, though the strength of nearly all the absorption lines (4200 Å features, S II, and Si II) is overestimated. $v_{\text{Si II}}$ is also overestimated ($\sim 12,000 \text{ km s}^{-1}$). When viewed from the opposite hemisphere from the helium detonation point (e.g., $\mu = -0.67$), the model yields an asymmetric profile of 4200 Å features that matches the observations better. The Si II features are also predicted to be shallower, though still not as shallow as that in the observations. Nonetheless, the spectra at early times are expected to be much bluer than the observations. The $\rho_5 = 14$ model has a thicker helium shell ($\sim 0.1 M_\odot$), and produces even shallower and slower-expanding Si II features at maximum brightness. This is in agreement with the trend observed in the right panel of Figure 5: models with a thicker helium shell tend to exhibit shallower Si II features. However, the level of line-blanketing blueward of $\sim 5000 \text{ Å}$ is also underestimated at early times. In addition, all three models, which have $M_{B,\text{max}} \simeq -19.3 \text{ mag}$, are not as bright as SN 2022joj.

To investigate the composition of the 4200 Å features at maximum luminosity, we take advantage of the 1D RT code TARDIS, which tracks back the last element that a photon interacts with (as emission/absorption) before escaping the photosphere, to approximate the results in the more realistic SEDONA 2D RT simulations conducted by (Shen et al. 2021b). [AAM: I am running another grid search to find the best fit – will include the plot soon. Also, we should ask Ken and Sam for some text explaining the 1D slices from their 2D sim-

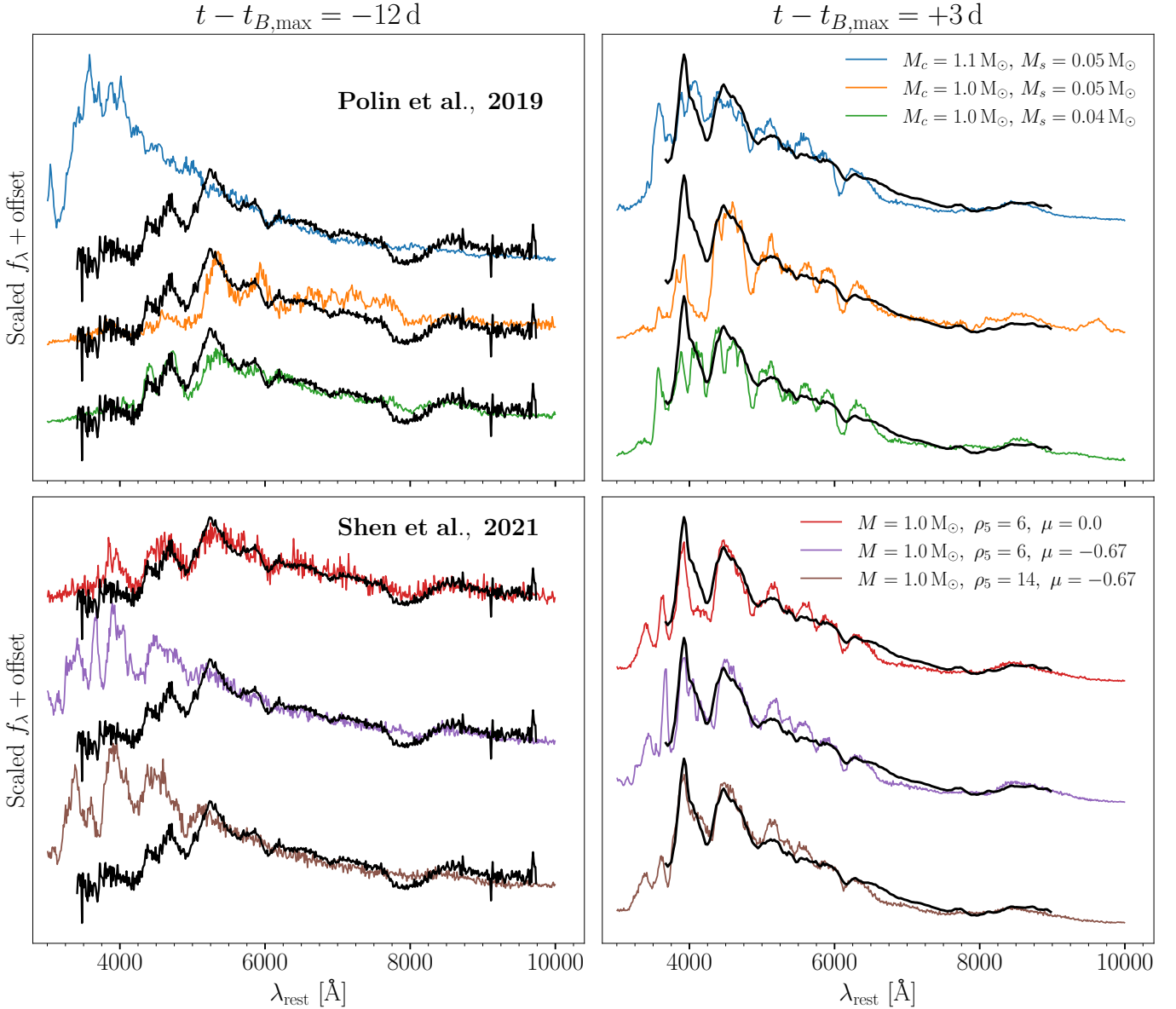


Figure 6. Comparisons of an early spectrum (~ -12 days) and a maximum-light spectrum ($\sim +3$ days) of SN 2022joj (black) with two sets of DDet models at corresponding phases. *Top*: results of 1D hydrodynamical simulations from Polin et al. (2019) with a variety of core masses (M_c) and shell masses (M_s). *Bottom*: results of 2D hydrodynamical simulations from (Shen et al. 2021b). A Galactic extinction of $E(B - V)_{\text{MW}}$ has been applied to each synthetic spectrum.

ulations.] We input a 1D slice near the viewing angle $\mu = 0$ in the $M = 1.0 M_\odot$ and $\rho_5 = 6$ model from Shen et al. (2021b) at the $t_{B,\text{max}}$ estimated in their 2D simulations. We find that with a low photospheric temperature ($T_{\text{ph}} \lesssim 8000$ K), the synthetic spectrum modeled by TARDIS could reproduce the spectroscopic features in the 2D RT results between ~ 3200 – 5500 Å. The blue edge of the 4200 Å features is dominated by the P-Cygni profile of the Ca H&K lines, while the asymmetric absorption profile is a result of a blend of Ti II, Co II, and Fe II lines. The strong line blanketing in the near-UV blueward of ~ 3500 Å is also a result of Ti, V, and

Cr absorption. However, we note that the optical luminosity in the TARDIS model is only $\sim 30\%$ of the yields from more realistic 2D RT simulations. Reproducing the luminosity in 2D results requires a higher photospheric temperature ($T_{\text{ph}} \gtrsim 10,000$ K), which would significantly alter the ionization in the ejecta. Specifically, at such a temperature the dominating Ti ions would be Ti III and the TARDIS model would fail to reproduce the 4200 Å features. We also find that none of our 1D RT models can reproduce the steep continuum redward of ~ 5500 Å in the synthetic spectra from Shen et al. (2021b). These inconsistencies result from the approxi-

mations made in TARDIS models, where a single photosphere is assumed for photons of different wavelengths, and multidimensional effects are not taken into account. Since the strong Ti II features and the shallow Si II features are simultaneously reproduced in 2D RT simulation, we conclude that this seemingly contradictory fact could be a result of RT in an asymmetric explosion.

We expect that a more massive 2D model may provide a better match to the observations. Unfortunately, there are only two models in Shen et al. (2021b) with progenitor masses $> 1 M_{\odot}$, and both have thin helium shells ($\lesssim 0.01 M_{\odot}$). These models therefore cannot reproduce the red color at ~ -12 days or the remarkable 4200 Å features at peak.

While none of the models presented here provide a strong match to SN 2022joj at every phase, we draw the broad conclusion that the spectroscopic properties of SN 2022joj are qualitatively consistent with a sub- M_{Ch} WD ($\gtrsim 1.0 M_{\odot}$) DDet viewed opposite from the shell ignition point. Observers from such a viewing angle would observe strong absorption features in the blue portion of the spectrum dominated by Ti II and IGEs as well as relatively shallow and slowly-expanding Si II lines in the red portion. We emphasize that none of the models considered here was specifically developed and tuned to explain SN 2022joj. Customized models specifically tuned for SN 2022joj may reproduce all the observed features simultaneously, and we suggest more 2D DDet simulations be performed. Additional improvements can be made via an improved handling of the radiative transfer (e.g., non-LTE effects; see Shen et al. 2021a).

4.2. The 7300 Å Region in Nebular-phase Spectra

In Figure 7 we compare the two nebular-phase spectra of SN 2022joj with the overluminous SNe Ia (SN 1991T, SN 1999aa, and SN 2018cnw) and the normal luminosity SN 2011fe.

Compared to other SNe Ia, the nebular spectra of SN 2022joj show a relatively low flux ratio between the complex at ~ 7300 Å (hereafter the 7300 Å features) and the [Fe III] 4700 Å features. This suggests high ionization in the ejecta (Wilk et al. 2020). In addition to the smaller flux ratio, the profile of the 7300 Å features in SN 2022joj is also distinct from other SNe. Most of SNe Ia show a bimodal structure in their 7300 Å features (e.g., Graham et al. 2017; Maguire et al. 2018). The bluer peak is dominated by [Fe II] $\lambda\lambda 7155, 7172$, while [Ni II] $\lambda\lambda 7378, 7412$ usually have non-negligible contributions to the redder peak (see Figure 7). In some peculiar SNe Ia (mostly subluminous ones), the detection of [Ca II] $\lambda\lambda 7291, 7324$ have also been reported (e.g. Jacobson-Galán et al. 2020; Siebert et al. 2020).

The bimodal morphology is prominent in the spectra of SN 1999aa and SN 2011fe. SN 1999T is well-known for its broader emission lines in the nebular phase, so the composition of the 7300 Å features is ambiguous. In the spectra of SN 2022joj and SN 2018cnw, however, the redder peak is absent and the 7300 Å features show an asymmetric single peak, which seems to indicate a low abundance of Ni in the ejecta.

To investigate the relative contributions of [Fe II] and [Ni II] to the 7300 Å features in SN 2022joj, we model this region with multiple Gaussian emission profiles using the same technique as in Section 3.3. We include four [Fe II] lines (7155, 7172, 7388, 7453 Å) and two [Ni II] lines (7378, 7412 Å) in the fit. For each species, the relative flux ratios of lines are fixed, whose values are adopted from Jerkstrand et al. (2015). For [Fe II], we set $L_{7155} : L_{7172} : L_{7388} : L_{7453} = 1 : 0.24 : 0.19 : 0.31$, and for [Ni II], we set $L_{7378} : L_{7412} = 1 : 0.31$. These line ratios are calculated assuming LTE, but the departure from LTE should not be significant under the typical conditions in the ejecta (Jerkstrand et al. 2015). We allow the amplitudes of these Gaussian profiles to be either positive or negative. The velocity dispersions in different lines of each species are set to be the same. For both the amplitudes and the logarithms of the velocity dispersion, we adopt a flat prior. In addition, we adopt wide Gaussian priors for the radial velocities of [Fe II] and [Ni II], both centered at -1000 km s^{-1} with a standard deviation of 2000 km s^{-1} . The fitted models are shown in Figure 8, where colored curves correspond to the [Fe II] and [Ni II] emission adopting the mean values of the posterior distributions of model parameters sampled with MCMC. In both spectra, the flux of [Ni II] is consistent with 0 ($L_{\text{Ni II}}/L_{\text{Fe II}} = 0.10 \pm 0.15$ at +287 days and 0.07 ± 0.16 at +330 days; the flux ratios of lines are estimated with the ratios of their pEWs), and the 7300 Å features can be well fit with [Fe II] emission only. We have also tested fitting this complex with [Ca II] in addition to [Fe II] and [Ni II], and we find no evidence for [Ca II].

The relative abundance of Ni and Fe, which probes the mass of the progenitor WD, can be estimated via the flux ratio of their emission lines. At >300 days after explosion ^{56}Fe is the dominant isotope of Fe following the decay of ^{56}Ni through the chain: $^{56}\text{Ni} \rightarrow ^{56}\text{Co} \rightarrow ^{56}\text{Fe}$. Consequently, the Fe abundance primarily depends on the yield of ^{56}Ni . The Ni abundance, however, is sensitive to both the progenitor mass and the explosion scenario. The stable Ni isotopes (^{58}Ni , ^{60}Ni , and ^{62}Ni) are more neutron-rich compared to the α -species ^{56}Ni , and can only be formed in high-density regions with an enhanced electron capture rate during the explosion

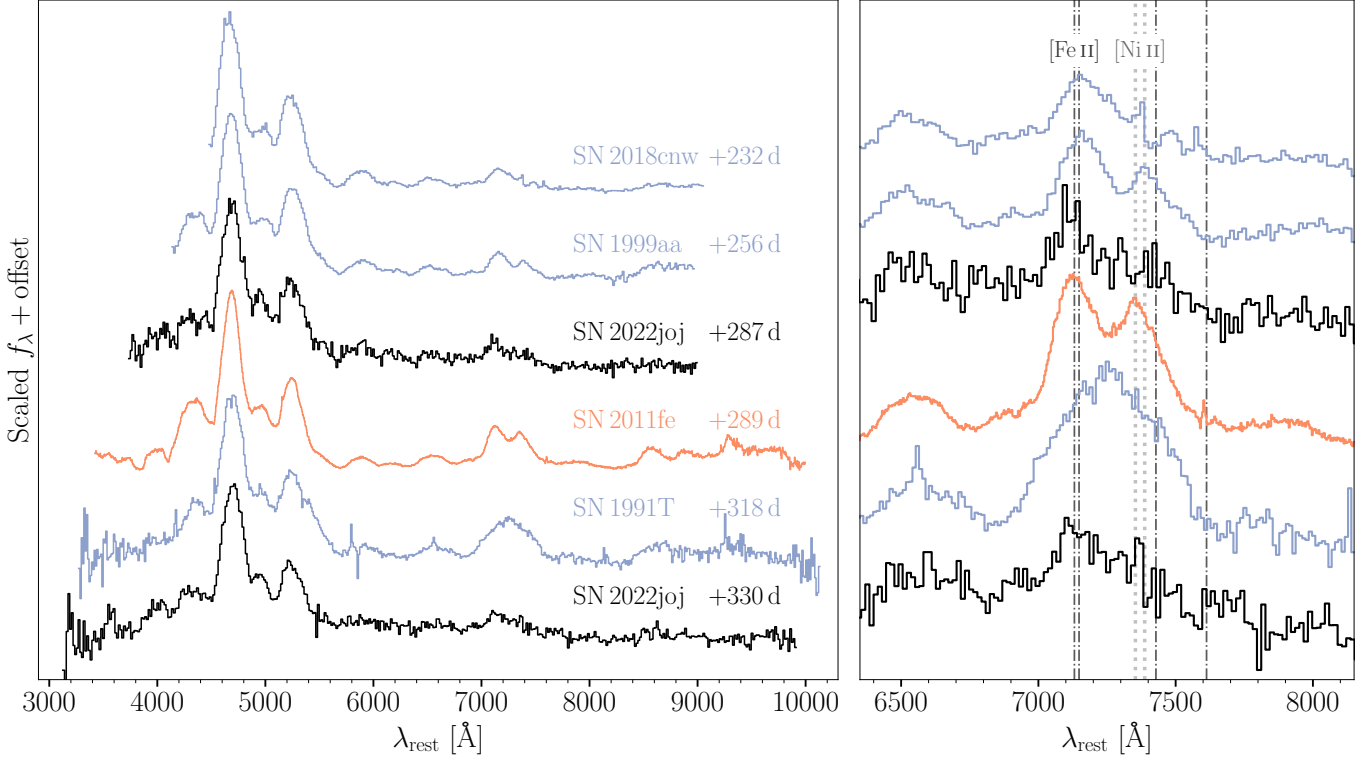


Figure 7. Nebular-phase spectra of SN 2022joj (black), three overluminous SNe Ia (blue), SN 1991T, SN 1999aa, and SN 2018cnw, and a normal SN Ia (orange), SN 2011fe. The right panel zooms in on the features around 7300 Å. The flux has been normalized to the [Fe III] features around 4700 Å. The dash-dotted lines correspond to wavelengths of four [Fe II] lines (7155 Å, 7172 Å, 7453 Å, and 7638 Å), while the dotted lines correspond to the wavelengths of two [Ni II] lines (7378 Å, 7412 Å), both blueshifted by 1000 km s⁻¹.

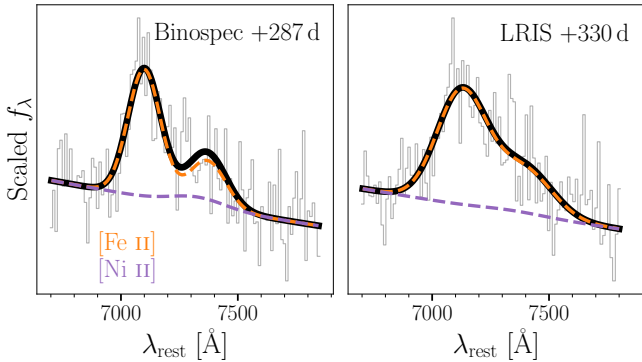


Figure 8. Fits to the 7300 Å region containing [Fe II] and [Ni II] features are consistent with a low Ni II abundance. The observed spectra are shown in grey. The dashed lines correspond to the models of [Fe II] (orange) and [Ni II] (purple) features. For the model parameters we adopt the mean values of their posterior distributions. The black solid lines are the overall models.

(Nomoto 1984; Khokhlov 1991). Consequently, SNe Ia from sub- M_{Ch} WDs, with central densities that are lower than near- M_{Ch} WDs, are expected to show a lower abundance of stable Ni isotopes (Iwamoto et al. 1999; Seitenzahl et al. 2013; Shen et al. 2018).

To estimate the relative abundance of Ni and Fe, we use the equation adopted in Jerkstrand et al. (2015) and Maguire et al. (2018),

$$\frac{L_{7378}}{L_{7155}} = 4.9 \frac{n_{\text{Ni II}}}{n_{\text{Fe II}}} \exp\left(\frac{0.28 \text{ eV}}{k_B T}\right) \frac{dc_{\text{Ni II}}}{dc_{\text{Fe II}}}, \quad (1)$$

where L_{7378}/L_{7155} is the flux ratio of the [Ni II] $\lambda 7378$ to [Fe II] $\lambda 7155$ lines, $n_{\text{Ni II}}$ ($n_{\text{Fe II}}$) is the number density of Ni II (Fe II), and $dc_{\text{Ni II}}/dc_{\text{Fe II}}$ is the ratio of the departure coefficients from LTE for these two ions. Since both Ni II and Fe II are singly ionized species with similar ionization potentials, we assume that $n_{\text{Ni II}}/n_{\text{Fe II}}$ is a good approximation of the total Ni/Fe ratio. As is illustrated in Maguire et al. (2018), this assumption proves to be valid by modeling nebular phase spectra at similar phases (Fransson & Jerkstrand 2015; Shingles et al. 2022), with the relative deviation from the ionization balance $\lesssim 20\%$. We handle the uncertainties due to the unknown temperature, ratio of departure coefficients, and the ionization balance in a Monte Carlo way. We randomly generate $N = 4000$ samples of the temperature (3000–8000 K), the ratio of departure coefficients (1.2–2.4), and the ionization balance factor (0.8–1.2) assuming uncorrelated uniform distributions. These inter-

vals are again adopted from Maguire et al. (2018). Combining these quantities with the samples of line profile parameters drawn with the MCMC, we obtain N estimates of Ni/Fe, which are effectively drawn from its posterior distribution. We find that Ni/Fe is consistent with 0 and we obtain a $3\text{-}\sigma$ upper limit of Ni/Fe < 0.04 . Such a low Ni abundance is more consistent with the yields of sub- M_{Ch} DDet scenarios (Shen et al. 2018), much lower than the expected outcomes of near- M_{Ch} , delayed detonation models (Seitenzahl et al. 2013) or pure deflagration models (Iwamoto et al. 1999).

Alternatively, it is proposed in Blondin et al. (2022) that for high-luminosity SNe Ia, the absence of [Ni II] lines is can be a result of high ionization of Ni in the inner ejecta, despite the fact that a significant amount of Ni exists. It is shown that the [Ni II] $\lambda\lambda 7378, 7412$ lines can be strongly suppressed even in a high luminosity, near- M_{Ch} delayed-detonation model, once the Ni II/Ni III ratio at the center of the ejecta is artificially reduced by a factor of 10. Nevertheless, it remains to be questioned if a physical mechanism exists to boost the ionization in the inner ejecta, where the stable Ni dominates the radioactive ^{56}Ni and ^{56}Co , and the deposited energy per particle due to the radioactive decay is usually low. One possible scenario is inward mixing, which brings ^{56}Co into the innermost ejecta such that the ionization would significantly increase. However, in this case Ca would inevitably be mixed inward as well, and the resultant Ca II $\lambda\lambda 7291, 7324$ lines would stand out and dominate the 7300 Å features (Blondin et al. 2022). Other physical mechanism are thus required to increase the Ni II/Ni III ratio at the center of a near- M_{Ch} explosion.

We also find that the [Fe II] lines are significantly blueshifted ($v_{[\text{Fe II}]} = -2.46 \pm 0.40 \text{ km s}^{-1}$ at +287 days and $-1.26 \pm 0.74 \text{ km s}^{-1}$ at +330 days). This is consistent with other SNe Ia showing low $v_{\text{Si II}}$ at maximum brightness (Maeda et al. 2010; Maguire et al. 2018; Li et al. 2021), and also in qualitative agreement with the asymmetric sub- M_{Ch} DDet scenarios. Specifically, along a line of sight opposite to the shell detonation point, observers would see intermediate mass elements (IMEs) with low expansion velocities, including Si II. In the meantime, the IGEs at the center of the ejecta would have a bulk velocity towards the observer (see Figure 1 and Figure 2 in Bulla et al. 2016; see also Fink et al. 2010).

5. CONCLUSIONS

We have presented observations of SN 2022joj, a peculiar, overluminous SNe Ia. SN 2022joj has an unusual color evolution, with a remarkably red $g_{\text{ZTF}} - r_{\text{ZTF}}$ color

at early times due to continuous absorption in the blue portion of its spectral energy distribution. Absorption features observed around maximum light simultaneously suggest high (a blue continuum, shallow Si II lines) and low (strong absorption around 4200 Å that may be associated with Ti II) photospheric temperatures. The nebular-phase spectra of SN 2022joj suggest a high ionization and low Ni abundance in the ejecta, consistent with a sub- M_{Ch} explosion.

The early red colors are most likely due to a layer of IGEs in the outermost ejecta as products of a helium-shell detonation, in the sub- M_{Ch} DDet scenario. If the asymmetric ejecta are observed opposite from the point of He shell ignition, we find that the resultant synthetic spectra could qualitatively reproduce some of the observed properties, including (i) significant line-blanking of flux due to IGEs at early phases; (ii) strong absorption features around 4200 Å as well as relatively weak Si II features near maximum brightness, and (iii) blueshifted [Fe II] $\lambda 7155$ accompanied with a relatively low expansion velocity of Si II at peak. No existing DDet model can fully explain all the observational properties of SN 2022joj. As a result, it is possible that some alternative model is superior, though we find the early red colors are difficult to explain with any other alternative explosion scenario. [Chang: as I write this sentence I realize we need to take a look at pulsational delayed detonations] [AAM: From Dessart et al. 2014, pulsational-delayed-detonation models tend to produce blue colors at early times, even for low mixing.] Future 2D models covering a finer grid of progenitor properties may answer the question if SN 2022joj is really a peculiar SN triggered by a DDet.

This work is based on observations obtained with the Samuel Oschin Telescope 48-inch and the 60-inch Telescope at the Palomar Observatory as part of the Zwicky Transient Facility project. ZTF is supported by the National Science Foundation under Grant No. AST-1440341 and a collaboration including Caltech, IPAC, the Weizmann Institute of Science, the Oskar Klein Center at Stockholm University, the University of Maryland, the University of Washington, Deutsches Elektronen-Synchrotron and Humboldt University, Los Alamos National Laboratories, the TANGO Consortium of Taiwan, the University of Wisconsin at Milwaukee, and Lawrence Berkeley National Laboratories. Operations are conducted by COO, IPAC, and UW. SED Machine is based upon work supported by the National Science Foundation under Grant No. 1106171.

This work is also based on observations made with the Nordic Optical Telescope, owned in collaboration

by the University of Turku and Aarhus University, and operated jointly by Aarhus University, the University of Turku and the University of Oslo, representing Denmark, Finland and Norway, the University of Iceland and Stockholm University at the Observatorio del Roque de los Muchachos, La Palma, Spain, of the Instituto de Astrofísica de Canarias.

The W. M. Keck Observatory is operated as a scientific partnership among the California Institute of Technology, the University of California and NASA; the observatory was made possible by the generous financial support of the W. M. Keck Foundation. Observations reported here were obtained at the MMT Observatory, a joint facility of the Smithsonian Institution and the Uni-

versity of Arizona. W. M. Keck Observatory and MMT Observatory access was supported by Northwestern University and the Center for Interdisciplinary Exploration and Research in Astrophysics (CIERA).

Facility: PO:1.2m (ZTF), PO:1.5m (SEDM), FTN (FLOYDS), FTS (FLOYDS), NOT (ALFOSC), Liverpool:2m (SPRAT), Keck:I (LRIS), MMT (Binospec).

Software: `astropy` (Astropy Collaboration et al. 2013, 2018), `matplotlib` (Hunter 2007), `NumPy` (Harris et al. 2020), `PyMC` (Salvatier et al. 2016), `PyteIt` (Prochaska et al. 2020), `pysedm` (Rigault et al. 2019), `SALT3` (Kenworthy et al. 2021), `sncosmo` (Barbary et al. 2023), `TARDIS` ()

REFERENCES

- Arbour, R., Papenkova, M., Li, W. D., Filippenko, A. V., & Armstrong, M. 1999, *IAUC*, 7156, 1
- Astropy Collaboration, Robitaille, T. P., Tollerud, E. J., et al. 2013, *A&A*, 558, A33, doi: [10.1051/0004-6361/201322068](https://doi.org/10.1051/0004-6361/201322068)
- Astropy Collaboration, Price-Whelan, A. M., Sipőcz, B. M., et al. 2018, *AJ*, 156, 123, doi: [10.3847/1538-3881/aabc4f](https://doi.org/10.3847/1538-3881/aabc4f)
- Barbary, K., Bailey, S., Barentsen, G., et al. 2023, *SNCosmo*, v2.10.0, Zenodo, doi: [10.5281/zenodo.7876632](https://doi.org/10.5281/zenodo.7876632)
- Bellm, E. C., Kulkarni, S. R., Graham, M. J., et al. 2019a, *PASP*, 131, 018002, doi: [10.1088/1538-3873/aaecbe](https://doi.org/10.1088/1538-3873/aaecbe)
- Bellm, E. C., Kulkarni, S. R., Barlow, T., et al. 2019b, *PASP*, 131, 068003, doi: [10.1088/1538-3873/ab0c2a](https://doi.org/10.1088/1538-3873/ab0c2a)
- Blagorodnova, N., Neill, J. D., Walters, R., et al. 2018, *PASP*, 130, 035003, doi: [10.1088/1538-3873/aaa53f](https://doi.org/10.1088/1538-3873/aaa53f)
- Blondin, S., Bravo, E., Timmes, F. X., Dessart, L., & Hillier, D. J. 2022, *A&A*, 660, A96, doi: [10.1051/0004-6361/202142323](https://doi.org/10.1051/0004-6361/202142323)
- Blondin, S., & Tonry, J. L. 2007, *ApJ*, 666, 1024, doi: [10.1086/520494](https://doi.org/10.1086/520494)
- Branch, D., Thomas, R. C., Baron, E., et al. 2004, *ApJ*, 606, 413, doi: [10.1086/382950](https://doi.org/10.1086/382950)
- Branch, D., Dang, L. C., Hall, N., et al. 2006, *PASP*, 118, 560, doi: [10.1086/502778](https://doi.org/10.1086/502778)
- Brown, P. J., Perry, J. M., Beeny, B. A., Milne, P. A., & Wang, X. 2018, *ApJ*, 867, 56, doi: [10.3847/1538-4357/aae1ad](https://doi.org/10.3847/1538-4357/aae1ad)
- Brown, T. M., Baliber, N., Bianco, F. B., et al. 2013, *PASP*, 125, 1031, doi: [10.1086/673168](https://doi.org/10.1086/673168)
- Bulla, M., Sim, S. A., Kromer, M., et al. 2016, *MNRAS*, 462, 1039, doi: [10.1093/mnras/stw1733](https://doi.org/10.1093/mnras/stw1733)
- Bulla, M., Miller, A. A., Yao, Y., et al. 2020, *ApJ*, 902, 48, doi: [10.3847/1538-4357/abb13c](https://doi.org/10.3847/1538-4357/abb13c)
- Burrow, A., Baron, E., Ashall, C., et al. 2020, *ApJ*, 901, 154, doi: [10.3847/1538-4357/abafa2](https://doi.org/10.3847/1538-4357/abafa2)
- Carrick, J., Turnbull, S. J., Lavaux, G., & Hudson, M. J. 2015, *MNRAS*, 450, 317, doi: [10.1093/mnras/stv547](https://doi.org/10.1093/mnras/stv547)
- Cenko, S. B., Fox, D. B., Moon, D.-S., et al. 2006, *PASP*, 118, 1396, doi: [10.1086/508366](https://doi.org/10.1086/508366)
- Childress, M. J., Filippenko, A. V., Ganeshalingam, M., & Schmidt, B. P. 2014, *MNRAS*, 437, 338, doi: [10.1093/mnras/stt1892](https://doi.org/10.1093/mnras/stt1892)
- Childress, M. J., Scalzo, R. A., Sim, S. A., et al. 2013, *ApJ*, 770, 29, doi: [10.1088/0004-637X/770/1/29](https://doi.org/10.1088/0004-637X/770/1/29)
- Chu, M., Dahiwal, A., & Fremling, C. 2022, *Transient Name Server Classification Report*, 2022-1458, 1
- De, K., Kasliwal, M. M., Polin, A., et al. 2019, *ApJ*, 873, L18, doi: [10.3847/2041-8213/ab0aec](https://doi.org/10.3847/2041-8213/ab0aec)
- De, K., Kasliwal, M. M., Tzanidakis, A., et al. 2020, *ApJ*, 905, 58, doi: [10.3847/1538-4357/abb45c](https://doi.org/10.3847/1538-4357/abb45c)
- de los Reyes, M. A. C., Kirby, E. N., Seitzzahl, I. R., & Shen, K. J. 2020, *ApJ*, 891, 85, doi: [10.3847/1538-4357/ab736f](https://doi.org/10.3847/1538-4357/ab736f)
- Dekany, R., Smith, R. M., Riddle, R., et al. 2020, *PASP*, 132, 038001, doi: [10.1088/1538-3873/ab4ca2](https://doi.org/10.1088/1538-3873/ab4ca2)
- Dessart, L., Blondin, S., Hillier, D. J., & Khokhlov, A. 2014, *MNRAS*, 441, 532, doi: [10.1093/mnras/stu598](https://doi.org/10.1093/mnras/stu598)
- Dey, A., Schlegel, D. J., Lang, D., et al. 2019, *AJ*, 157, 168, doi: [10.3847/1538-3881/ab089d](https://doi.org/10.3847/1538-3881/ab089d)
- Dong, Y., Valenti, S., Polin, A., et al. 2022, *ApJ*, 934, 102, doi: [10.3847/1538-4357/ac75eb](https://doi.org/10.3847/1538-4357/ac75eb)
- Duev, D. A., Mahabal, A., Masci, F. J., et al. 2019, *MNRAS*, 489, 3582, doi: [10.1093/mnras/stz2357](https://doi.org/10.1093/mnras/stz2357)
- Eitner, P., Bergemann, M., Ruiter, A. J., et al. 2022, *arXiv e-prints*, arXiv:2206.10258, <https://arxiv.org/abs/2206.10258>

- Fabricant, D., Fata, R., Epps, H., et al. 2019, *PASP*, 131, 075004, doi: [10.1088/1538-3873/ab1d78](https://doi.org/10.1088/1538-3873/ab1d78)
- Filippenko, A. V., Richmond, M. W., Matheson, T., et al. 1992a, *ApJL*, 384, L15, doi: [10.1086/186252](https://doi.org/10.1086/186252)
- Filippenko, A. V., Richmond, M. W., Branch, D., et al. 1992b, *AJ*, 104, 1543, doi: [10.1086/116339](https://doi.org/10.1086/116339)
- Fink, M., Röpke, F. K., Hillebrandt, W., et al. 2010, *A&A*, 514, A53, doi: [10.1051/0004-6361/200913892](https://doi.org/10.1051/0004-6361/200913892)
- Fitzpatrick, E. L. 1999, *PASP*, 111, 63, doi: [10.1086/316293](https://doi.org/10.1086/316293)
- Flörs, A., Spyromilio, J., Taubenberger, S., et al. 2020, *MNRAS*, 491, 2902, doi: [10.1093/mnras/stz3013](https://doi.org/10.1093/mnras/stz3013)
- Fransson, C., & Jerkstrand, A. 2015, *ApJL*, 814, L2, doi: [10.1088/2041-8205/814/1/L2](https://doi.org/10.1088/2041-8205/814/1/L2)
- Fremling, C. 2022, *Transient Name Server Discovery Report*, 2022-1220, 1
- Galbany, L., Ashall, C., Hflich, P., et al. 2019, *A&A*, 630, A76, doi: [10.1051/0004-6361/201935537](https://doi.org/10.1051/0004-6361/201935537)
- Garavini, G., Folatelli, G., Goobar, A., et al. 2004, *AJ*, 128, 387, doi: [10.1086/421747](https://doi.org/10.1086/421747)
- Gehrels, N., Chincarini, G., Giommi, P., et al. 2004, *ApJ*, 611, 1005, doi: [10.1086/422091](https://doi.org/10.1086/422091)
- Graham, M. J., Kulkarni, S. R., Bellm, E. C., et al. 2019, *PASP*, 131, 078001, doi: [10.1088/1538-3873/ab006c](https://doi.org/10.1088/1538-3873/ab006c)
- Graham, M. L., Kumar, S., Hosseinzadeh, G., et al. 2017, *MNRAS*, 472, 3437, doi: [10.1093/mnras/stx2224](https://doi.org/10.1093/mnras/stx2224)
- Harris, C. R., Millman, K. J., van der Walt, S. J., et al. 2020, *Nature*, 585, 357, doi: [10.1038/s41586-020-2649-2](https://doi.org/10.1038/s41586-020-2649-2)
- HEASARC. 2014, *HEASoft: Unified Release of FTOOLS and XANADU*, Astrophysics Source Code Library, record ascl:1408.004. <http://ascl.net/1408.004>
- Hunter, J. D. 2007, *Computing in Science and Engineering*, 9, 90, doi: [10.1109/MCSE.2007.55](https://doi.org/10.1109/MCSE.2007.55)
- Insera, C., Sim, S. A., Wyrzykowski, L., et al. 2015, *ApJL*, 799, L2, doi: [10.1088/2041-8205/799/1/L2](https://doi.org/10.1088/2041-8205/799/1/L2)
- Iwamoto, K., Brachwitz, F., Nomoto, K., et al. 1999, *ApJS*, 125, 439, doi: [10.1086/313278](https://doi.org/10.1086/313278)
- Jacobson-Galán, W. V., Polin, A., Foley, R. J., et al. 2020, *ApJ*, 896, 165, doi: [10.3847/1538-4357/ab94b8](https://doi.org/10.3847/1538-4357/ab94b8)
- Jerkstrand, A., Smartt, S. J., Sollerman, J., et al. 2015, *MNRAS*, 448, 2482, doi: [10.1093/mnras/stv087](https://doi.org/10.1093/mnras/stv087)
- Jiang, J.-a., Doi, M., Maeda, K., et al. 2017, *Nature*, 550, 80, doi: [10.1038/nature23908](https://doi.org/10.1038/nature23908)
- Kasen, D. 2010, *ApJ*, 708, 1025, doi: [10.1088/0004-637X/708/2/1025](https://doi.org/10.1088/0004-637X/708/2/1025)
- Kenworthy, W. D., Jones, D. O., Dai, M., et al. 2021, *ApJ*, 923, 265, doi: [10.3847/1538-4357/ac30d8](https://doi.org/10.3847/1538-4357/ac30d8)
- Khokhlov, A. M. 1991, *A&A*, 245, L25
- Kromer, M., Sim, S. A., Fink, M., et al. 2010, *ApJ*, 719, 1067, doi: [10.1088/0004-637X/719/2/1067](https://doi.org/10.1088/0004-637X/719/2/1067)
- Leibundgut, B., Kirshner, R. P., Phillips, M. M., et al. 1993, *AJ*, 105, 301, doi: [10.1086/116427](https://doi.org/10.1086/116427)
- Li, W., Wang, X., Bulla, M., et al. 2021, *ApJ*, 906, 99, doi: [10.3847/1538-4357/abc9b5](https://doi.org/10.3847/1538-4357/abc9b5)
- Lira, P. 1996, *Master's thesis*, -
- Liu, C., Miller, A. A., Polin, A., et al. 2023a, *ApJ*, 946, 83, doi: [10.3847/1538-4357/acbb5e](https://doi.org/10.3847/1538-4357/acbb5e)
- Liu, Z.-W., Roepke, F. K., & Han, Z. 2023b, *arXiv e-prints*, arXiv:2305.13305, doi: [10.48550/arXiv.2305.13305](https://doi.org/10.48550/arXiv.2305.13305)
- Livne, E. 1990, *ApJL*, 354, L53, doi: [10.1086/185721](https://doi.org/10.1086/185721)
- Livne, E., & Arnett, D. 1995, *ApJ*, 452, 62, doi: [10.1086/176279](https://doi.org/10.1086/176279)
- Maeda, K., Benetti, S., Stritzinger, M., et al. 2010, *Nature*, 466, 82, doi: [10.1038/nature09122](https://doi.org/10.1038/nature09122)
- Magee, M. R., & Maguire, K. 2020, *A&A*, 642, A189, doi: [10.1051/0004-6361/202037870](https://doi.org/10.1051/0004-6361/202037870)
- Magee, M. R., Maguire, K., Kotak, R., & Sim, S. A. 2021, *MNRAS*, 502, 3533, doi: [10.1093/mnras/stab201](https://doi.org/10.1093/mnras/stab201)
- Maguire, K., Sullivan, M., Pan, Y. C., et al. 2014, *MNRAS*, 444, 3258, doi: [10.1093/mnras/stu1607](https://doi.org/10.1093/mnras/stu1607)
- Maguire, K., Sim, S. A., Shingles, L., et al. 2018, *MNRAS*, 477, 3567, doi: [10.1093/mnras/sty820](https://doi.org/10.1093/mnras/sty820)
- Mahabal, A., Rebbapragada, U., Walters, R., et al. 2019, *PASP*, 131, 038002, doi: [10.1088/1538-3873/aaf3fa](https://doi.org/10.1088/1538-3873/aaf3fa)
- Maoz, D., Mannucci, F., & Nelemans, G. 2014, *ARA&A*, 52, 107, doi: [10.1146/annurev-astro-082812-141031](https://doi.org/10.1146/annurev-astro-082812-141031)
- Masci, F. J., Laher, R. R., Rusholme, B., et al. 2023, *arXiv e-prints*, arXiv:2305.16279, doi: [10.48550/arXiv.2305.16279](https://doi.org/10.48550/arXiv.2305.16279)
- . 2019, *PASP*, 131, 018003, doi: [10.1088/1538-3873/aae8ac](https://doi.org/10.1088/1538-3873/aae8ac)
- Matheson, T., Filippenko, A. V., Barth, A. J., et al. 2000, *AJ*, 120, 1487, doi: [10.1086/301518](https://doi.org/10.1086/301518)
- Matheson, T., Kirshner, R. P., Challis, P., et al. 2008, *AJ*, 135, 1598, doi: [10.1088/0004-6256/135/4/1598](https://doi.org/10.1088/0004-6256/135/4/1598)
- Mazzali, P. A., Chugai, N., Turatto, M., et al. 1997, *MNRAS*, 284, 151, doi: [10.1093/mnras/284.1.151](https://doi.org/10.1093/mnras/284.1.151)
- Miller, A. A., Yao, Y., Bulla, M., et al. 2020, *ApJ*, 902, 47, doi: [10.3847/1538-4357/abb13b](https://doi.org/10.3847/1538-4357/abb13b)
- Newsome, M., Li, W., Burke, J., et al. 2022, *Transient Name Server Classification Report*, 2022-1274, 1
- Ni, Y. Q., Moon, D.-S., Drouot, M. R., et al. 2022, *Nature Astronomy*, 6, 568, doi: [10.1038/s41550-022-01603-4](https://doi.org/10.1038/s41550-022-01603-4)
- . 2023, *ApJ*, 946, 7, doi: [10.3847/1538-4357/aca9be](https://doi.org/10.3847/1538-4357/aca9be)
- Noebauer, U. M., Kromer, M., Taubenberger, S., et al. 2017, *MNRAS*, 472, 2787, doi: [10.1093/mnras/stx2093](https://doi.org/10.1093/mnras/stx2093)
- Nomoto, K. 1982a, *ApJ*, 253, 798, doi: [10.1086/159682](https://doi.org/10.1086/159682)
- . 1982b, *ApJ*, 257, 780, doi: [10.1086/160031](https://doi.org/10.1086/160031)
- . 1984, *ApJ*, 277, 791, doi: [10.1086/161749](https://doi.org/10.1086/161749)

- Oke, J. B., Cohen, J. G., Carr, M., et al. 1995, *PASP*, 107, 375, doi: [10.1086/133562](https://doi.org/10.1086/133562)
- Padilla Gonzalez, E., Howell, D. A., Burke, J., et al. 2023, arXiv e-prints, arXiv:2305.07708, doi: [10.48550/arXiv.2305.07708](https://doi.org/10.48550/arXiv.2305.07708)
- Patterson, M. T., Bellm, E. C., Rusholme, B., et al. 2019, *PASP*, 131, 018001, doi: [10.1088/1538-3873/aae904](https://doi.org/10.1088/1538-3873/aae904)
- Pereira, R., Thomas, R. C., Aldering, G., et al. 2013, *A&A*, 554, A27, doi: [10.1051/0004-6361/201221008](https://doi.org/10.1051/0004-6361/201221008)
- Phillips, A. C., Miller, J., Cowley, D., & Wallace, V. 2006, in *Society of Photo-Optical Instrumentation Engineers (SPIE) Conference Series*, Vol. 6269, Society of Photo-Optical Instrumentation Engineers (SPIE) Conference Series, ed. I. S. McLean & M. Iye, 62691O, doi: [10.1117/12.672469](https://doi.org/10.1117/12.672469)
- Phillips, M. M., Lira, P., Suntzeff, N. B., et al. 1999, *AJ*, 118, 1766, doi: [10.1086/301032](https://doi.org/10.1086/301032)
- Piasecik, A. S., Steele, I. A., Bates, S. D., et al. 2014, in *Society of Photo-Optical Instrumentation Engineers (SPIE) Conference Series*, Vol. 9147, Ground-based and Airborne Instrumentation for Astronomy V, ed. S. K. Ramsay, I. S. McLean, & H. Takami, 91478H, doi: [10.1117/12.2055117](https://doi.org/10.1117/12.2055117)
- Piro, A. L., & Morozova, V. S. 2016, *ApJ*, 826, 96, doi: [10.3847/0004-637X/826/1/96](https://doi.org/10.3847/0004-637X/826/1/96)
- Piro, A. L., & Nakar, E. 2013, *ApJ*, 769, 67, doi: [10.1088/0004-637X/769/1/67](https://doi.org/10.1088/0004-637X/769/1/67)
- Polin, A., Nugent, P., & Kasen, D. 2019, *ApJ*, 873, 84, doi: [10.3847/1538-4357/aafb6a](https://doi.org/10.3847/1538-4357/aafb6a)
- Poole, T. S., Breeveld, A. A., Page, M. J., et al. 2008, *MNRAS*, 383, 627, doi: [10.1111/j.1365-2966.2007.12563.x](https://doi.org/10.1111/j.1365-2966.2007.12563.x)
- Prochaska, J. X., Hennawi, J. F., Westfall, K. B., et al. 2020, *Journal of Open Source Software*, 5, 2308, doi: [10.21105/joss.02308](https://doi.org/10.21105/joss.02308)
- Prochaska, J. X., Hennawi, J., Cooke, R., et al. 2020, *pypeit/PypeIt: Release 1.0.0, v1.0.0*, Zenodo, doi: [10.5281/zenodo.3743493](https://doi.org/10.5281/zenodo.3743493)
- Rigault, M., Neill, J. D., Blagorodnova, N., et al. 2019, *A&A*, 627, A115, doi: [10.1051/0004-6361/201935344](https://doi.org/10.1051/0004-6361/201935344)
- Roming, P. W. A., Kennedy, T. E., Mason, K. O., et al. 2005, *SSRv*, 120, 95, doi: [10.1007/s11214-005-5095-4](https://doi.org/10.1007/s11214-005-5095-4)
- Salvatier, J., Wiecki, T. V., & Fonnesbeck, C. 2016, *PeerJ Computer Science*, 2, e55, doi: [10.7717/peerj-cs.55](https://doi.org/10.7717/peerj-cs.55)
- Sanders, J. L., Belokurov, V., & Man, K. T. F. 2021, *MNRAS*, 506, 4321, doi: [10.1093/mnras/stab1951](https://doi.org/10.1093/mnras/stab1951)
- Schlaflly, E. F., & Finkbeiner, D. P. 2011, *ApJ*, 737, 103, doi: [10.1088/0004-637X/737/2/103](https://doi.org/10.1088/0004-637X/737/2/103)
- Seitenzahl, I. R., Ciaraldi-Schoolmann, F., Röpke, F. K., et al. 2013, *MNRAS*, 429, 1156, doi: [10.1093/mnras/sts402](https://doi.org/10.1093/mnras/sts402)
- Shen, K. J., Blondin, S., Kasen, D., et al. 2021a, *ApJL*, 909, L18, doi: [10.3847/2041-8213/abe69b](https://doi.org/10.3847/2041-8213/abe69b)
- Shen, K. J., Boos, S. J., Townsley, D. M., & Kasen, D. 2021b, *ApJ*, 922, 68, doi: [10.3847/1538-4357/ac2304](https://doi.org/10.3847/1538-4357/ac2304)
- Shen, K. J., Kasen, D., Miles, B. J., & Townsley, D. M. 2018, *ApJ*, 854, 52, doi: [10.3847/1538-4357/aaa8de](https://doi.org/10.3847/1538-4357/aaa8de)
- Shingles, L. J., Flörs, A., Sim, S. A., et al. 2022, *MNRAS*, 512, 6150, doi: [10.1093/mnras/stac902](https://doi.org/10.1093/mnras/stac902)
- Siebert, M. R., Dimitriadis, G., Polin, A., & Foley, R. J. 2020, *ApJL*, 900, L27, doi: [10.3847/2041-8213/abae6e](https://doi.org/10.3847/2041-8213/abae6e)
- Silverman, J. M., Foley, R. J., Filippenko, A. V., et al. 2012, *MNRAS*, 425, 1789, doi: [10.1111/j.1365-2966.2012.21270.x](https://doi.org/10.1111/j.1365-2966.2012.21270.x)
- Steele, I. A., Smith, R. J., Rees, P. C., et al. 2004, in *Society of Photo-Optical Instrumentation Engineers (SPIE) Conference Series*, Vol. 5489, Ground-based Telescopes, ed. J. Oschmann, Jacobus M., 679–692, doi: [10.1117/12.551456](https://doi.org/10.1117/12.551456)
- Taubenberger, S. 2017, in *Handbook of Supernovae*, ed. A. W. Alsabti & P. Murdin (Springer), 317, doi: [10.1007/978-3-319-21846-5_37](https://doi.org/10.1007/978-3-319-21846-5_37)
- Tonry, J. L., Denneau, L., Heinze, A. N., et al. 2018, *PASP*, 130, 064505, doi: [10.1088/1538-3873/aabadf](https://doi.org/10.1088/1538-3873/aabadf)
- Townsley, D. M., Miles, B. J., Shen, K. J., & Kasen, D. 2019, *ApJL*, 878, L38, doi: [10.3847/2041-8213/ab27cd](https://doi.org/10.3847/2041-8213/ab27cd)
- Wilk, K. D., Hillier, D. J., & Dessart, L. 2020, *MNRAS*, 494, 2221, doi: [10.1093/mnras/staa640](https://doi.org/10.1093/mnras/staa640)
- Woosley, S. E., Taam, R. E., & Weaver, T. A. 1986, *ApJ*, 301, 601, doi: [10.1086/163926](https://doi.org/10.1086/163926)
- Woosley, S. E., & Weaver, T. A. 1994, *ApJ*, 423, 371, doi: [10.1086/173813](https://doi.org/10.1086/173813)
- Yao, Y., Miller, A. A., Kulkarni, S. R., et al. 2019, *ApJ*, 886, 152, doi: [10.3847/1538-4357/ab4cf5](https://doi.org/10.3847/1538-4357/ab4cf5)
- Yaron, O., & Gal-Yam, A. 2012, *PASP*, 124, 668, doi: [10.1086/666656](https://doi.org/10.1086/666656)
- Zackay, B., Ofek, E. O., & Gal-Yam, A. 2016, *ApJ*, 830, 27, doi: [10.3847/0004-637X/830/1/27](https://doi.org/10.3847/0004-637X/830/1/27)
- Zheng, W., Kelly, P. L., & Filippenko, A. V. 2018, *ApJ*, 858, 104, doi: [10.3847/1538-4357/aabaeb](https://doi.org/10.3847/1538-4357/aabaeb)